

## In Situ Observations of Madden–Julian Oscillation Mixed Layer Dynamics in the Indian and Western Pacific Oceans

KYLA DRUSHKA,\* JANET SPRINTALL, AND SARAH T. GILLE

*Scripps Institution of Oceanography, La Jolla, California*

SUSAN WIJFFELS

*Center for Australian Weather and Climate Research, CSIRO Marine and Atmospheric Research,  
Hobart, Tasmania, Australia*

(Manuscript received 14 April 2011, in final form 22 August 2011)

### ABSTRACT

The boreal winter response of the ocean mixed layer to the Madden–Julian oscillation (MJO) in the Indo-Pacific region is determined using in situ observations from the Argo profiling float dataset. Composite averages over numerous events reveal that the MJO forces systematic variations in mixed layer depth and temperature throughout the domain. Strong MJO mixed layer depth anomalies ( $>15$  m peak to peak) are observed in the central Indian Ocean and in the far western Pacific Ocean. The strongest mixed layer temperature variations ( $>0.6^{\circ}\text{C}$  peak to peak) are found in the central Indian Ocean and in the region between northwest Australia and Java. A heat budget analysis is used to evaluate which processes are responsible for mixed layer temperature variations at MJO time scales. Though uncertainties in the heat budget are on the same order as the temperature trend, the analysis nonetheless demonstrates that mixed layer temperature variations associated with the canonical MJO are driven largely by anomalous net surface heat flux. Net heat flux is dominated by anomalies in shortwave and latent heat fluxes, the relative importance of which varies between active and suppressed MJO conditions. Additionally, rapid deepening of the mixed layer in the central Indian Ocean during the onset of active MJO conditions induces significant basin-wide entrainment cooling. In the central equatorial Indian Ocean, MJO-induced variations in mixed layer depth can modulate net surface heat flux, and therefore mixed layer temperature variations, by up to  $\sim 40\%$ . This highlights the importance of correctly representing intraseasonal mixed layer depth variations in climate models in order to accurately simulate mixed layer temperature, and thus air–sea interaction, associated with the MJO.

### 1. Introduction

The Madden–Julian oscillation (MJO) is a system of large-scale coupled patterns of atmospheric convection and winds that originate in the western tropical Indian Ocean, propagate eastward along the equator, and eventually die out in the eastern Pacific Ocean (Madden and Julian 1972). Atmospheric MJO forcing exerts a profound influence on the mixed layer of the tropical Indian and Pacific Oceans through anomalous fluxes of

heat, precipitation, and momentum (e.g., Hendon and Glick 1997; Lau and Waliser 2005). In turn, these processes affect the distribution of heat and salt in the ocean mixed layer. The impacts of the MJO on weather and climate are manifold (e.g., see the thorough review by Zhang 2005), most notably in the tropical Indian and Pacific Oceans where the forcing is strongest, but also globally. Despite extensive study, model simulations consistently fail to reproduce the MJO correctly, and MJO forecasts are not accurate beyond around two weeks (Seo et al. 2009). As a result, the impacts of the MJO on both present-day and future weather and climate are still largely unresolved.

Results from model sensitivity tests have suggested that air–sea coupling is an integral part of MJO dynamics (e.g., Flatau et al. 1997; Waliser et al. 1999; Inness and Slingo 2003; Maloney and Sobel 2004; Woolnough et al. 2007). Developing a better picture for how MJO forcing

\* Current affiliation: Laboratoire d’Océanographie Expérimentation et Approches Numériques, Paris, France.

Corresponding author address: Kyla Drushka, Laboratoire d’Océanographie Expérimentation et Approches Numériques, 4, place Jussieu, 75252 Paris CEDEX 05, France.  
E-mail: kyla.drushka@locean-ipsl.upmc.fr

impacts the ocean, and how this may feed back onto the MJO, may thus be necessary for improving MJO prediction and modeling. This requires quantifying not only the variations associated with the MJO at the air-sea interface, but also the variations within the upper ocean.

The MJO can force significant fluctuations in the mixed layer depth (MLD; e.g., Lukas and Lindstrom 1991; Shinoda and Hendon 1998; Waliser et al. 2003; Duvel et al. 2004). Since heat, freshwater, and momentum inputs are integrated over the mixed layer, variations in MLD could modulate the impacts of surface forcing. There have been relatively few water column observations available at time scales sufficient for capturing MJO variability. Consequently, previous studies of how the MJO influences the ocean have generally used model output (e.g., Schiller and Godfrey 2003; Waliser et al. 2003; Duvel et al. 2004; Lucas et al. 2010) or relied only on satellite observations (e.g., Duvel and Vialard 2007). Those studies that did include in situ subsurface observations have primarily been limited to mooring sites (e.g., Anderson et al. 1996; Zhang and McPhaden 2000; Vialard et al. 2008) or the inclusion of Argo profiling floats in a small regional domain (e.g., Han et al. 2007; Vinayachandran and Saji 2008; Sato et al. 2011), and very few studies have used in situ observations to characterize the MJO signal over a large domain. Matthews et al. (2010) used Argo data to characterize MJO-related anomalies of temperature and salinity throughout the water column. This study revealed that patterns of anomalous mixed layer temperature in the Indian and western Pacific Oceans are consistent with being forced by anomalies in heat flux that arise from MJO convective and wind anomalies. In addition, Matthews et al. (2010) showed that subsurface salinity variations at MJO time scales, which are dominated by anomalies in precipitation minus evaporation in the Indian Ocean and zonal advection in the western Pacific Ocean, have different spatial and temporal characteristics than those of temperature. This implies that there may be variations in the upper-ocean density structure, and thus MLD, at MJO time scales.

In the present study, we use data from Argo profiling floats to characterize the upper-ocean response to the MJO. Whereas Matthews et al. (2010) focused on quantifying the MJO temperature and salinity anomalies throughout the water column, the aim of the present study is 1) to quantify variations in MLD forced by the MJO, and 2) to use an upper-ocean heat budget analysis to determine what drives changes in mixed layer temperature at MJO time scales. We do this using composites of MJO anomalies based on the index of Wheeler and Hendon (2004) (i.e., the “Wheeler–Hendon index”). The Wheeler–Hendon index breaks the MJO cycle into eight phases that correspond to the shifting location of maximum intraseasonal winds and convection, so composites

formed using this index describe the response of the atmosphere and upper ocean to the MJO as it moves eastward over the Indian Ocean and through the Pacific Ocean. From Argo observations of subsurface temperature and salinity, we estimate MLD and vertical temperature gradients, and construct composite MJO mixed layer heat budgets. Although our estimates are not sufficiently accurate to close the heat budget, we use the composites to qualitatively expand on the existing picture of how MJO forcing impacts the upper ocean, with a particular emphasis on the role of MLD variations.

The paper is organized as follows: in section 2 we describe the datasets used in the study and the method used to estimate MJO signals. The composite forcing and mixed layer response (including a heat budget analysis) are presented in section 3, and the effect of MJO-related MLD variations on the heat budget is shown in section 4. In section 5 we discuss sources of uncertainty in the analysis, including a comparison of four heat flux products. The findings are summarized in section 6.

## 2. Data and methodology

### a. Heat budgets

The “active” MJO is characterized by the presence of a deep convective anomaly with a zonal wavelength of  $12\,000 \sim 20\,000$  km that is coupled to zonal surface wind anomalies (Wheeler and Hendon 2004). The whole system propagates eastward along the equator at around  $5\text{ m s}^{-1}$  (Zhang 2005). To the east and west of the active MJO, convection and winds are anomalously weak: this characterizes the inactive, or suppressed, MJO phase. Atmospheric forcing during MJO events affects the ocean mixed layer in various ways. Convective cells block the incoming solar radiation from reaching the sea surface, producing anomalously cool sea surface temperatures (SSTs; e.g., Hendon and Glick 1997; Shinoda et al. 1998). Wind anomalies associated with the MJO have numerous impacts (Cronin and McPhaden 1997, and references therein). Increased wind stress cools the sea surface by enhancing latent heat loss (Zhang and McPhaden 1995). Strong winds can also induce localized vertical entrainment, which has been shown to contribute significantly to (McPhaden 2002; Schiller and Godfrey 2003; Saji et al. 2006; Jayakumar et al. 2011) or even dominate (Duncan and Han 2009), changes in mixed layer temperature. Vertical velocities, for example due to anomalies in Ekman pumping, can vertically advect heat into or out of the mixed layer (Sato et al. 2011). Finally, wind bursts can force both ocean currents that advect heat horizontally (e.g., Waliser et al. 2003; Lau and Waliser 2005; Cronin and McPhaden 1997), as well as equatorial

waves that cause propagating anomalies in thermocline depth (Lucas et al. 2010). To diagnose the relative impacts of these processes on the mixed layer temperature, we estimated a mixed layer heat budget, which can be expressed as (e.g., Schiller and Godfrey 2003; Jayakumar et al. 2011)

$$\frac{\partial T}{\partial t} = \underbrace{\frac{Q_o}{\rho c_p h}}_a - \underbrace{\left( u \frac{\partial T}{\partial x} + v \frac{\partial T}{\partial y} \right)}_b - \underbrace{w_{Ek} \frac{\partial T}{\partial z} - \frac{\partial h \Delta T}{\partial t} \mathcal{H}}_c - \epsilon. \quad (1)$$

The right-hand side of Eq. (1) describes the different contributions to variations in mixed layer temperature ( $T$ ). Term  $a$ , referred to as the corrected net heat flux forcing, is the total heat flux into the mixed layer ( $Q_o$ ) that has been scaled by the MLD,  $h$ , and the volumetric heat capacity of seawater,  $\rho c_p$ . Here  $Q_o$  is equal to the sum of the shortwave, longwave, sensible, and latent heat fluxes and is corrected for  $Q_{pen}$ , the amount of shortwave radiation that penetrates through the bottom of the mixed layer and thus does not contribute to the heating ( $Q_o = Q_{net} - Q_{pen} = Q_{sw} + Q_{lw} + Q_{sh} + Q_{lh} - Q_{pen}$ , where we have followed the convention that heat flux terms are positive when they warm the mixed layer).

Term  $b$  represents the horizontal advection of heat into the mixed layer:  $u$  and  $v$  are the zonal and meridional surface currents, respectively; and  $\partial T/\partial x$  and  $\partial T/\partial y$  are the zonal and meridional temperature gradients, respectively. Term  $c$  describes the vertical fluxes of heat: advection (assumed to result from Ekman pumping) and vertical entrainment of deeper water into the mixed layer. Here  $w_{Ek}$  is the vertical Ekman velocity and  $\Delta T$  is the temperature difference between water within and just below the mixed layer. The vertical entrainment term is multiplied by the Heaviside function  $\mathcal{H}$ , which is equal to zero for a shoaling mixed layer ( $\partial h/\partial t \leq 0$ ) and equal to 1 for a deepening mixed layer ( $\partial h/\partial t > 0$ ). The residual  $\epsilon$  includes turbulent entrainment and mixing at the base of the mixed layer, diffusion, advection from vertical velocities other than Ekman pumping, and errors.

Anomalies excited by the MJO are superimposed on the background state of the ocean, so it is necessary to consider all interactions between background conditions and anomalies forced by the MJO. For example, horizontal advection involves anomalous MJO currents acting on both the mean and MJO temperature gradients, as well as the mean current acting on anomalous temperature gradients that arise due to the MJO. For each term (“ $X$ ”) in Eq. (1), the time-mean ( $\bar{X}$ ) and the MJO ( $\hat{X}$ ) components can be separated out. Then, the MJO heat budget can be expressed as

$$\begin{aligned} \frac{\partial \hat{T}}{\partial t} = & \left[ \frac{\overline{Q}_o + \hat{Q}_o}{\rho c_p (\bar{h} + \hat{h})} \right] - \left[ \frac{\overline{Q}_o + \hat{Q}_o}{\rho c_p (\bar{h} + \hat{h})} \right] - (\bar{\mathbf{u}} \cdot \nabla \hat{T} + \hat{\mathbf{u}} \cdot \nabla \bar{T} + \hat{\mathbf{u}} \cdot \nabla \bar{T}) \\ & - \left( \bar{w}_{Ek} \frac{\partial \bar{T}}{\partial z} + \hat{w}_{Ek} \frac{\partial \bar{T}}{\partial z} + \hat{w}_{Ek} \frac{\partial \hat{T}}{\partial z} \right) - \left[ \frac{\frac{\partial \hat{h}}{\partial t} \Delta T}{\bar{h} + \hat{h}} - \left( \frac{\frac{\partial \hat{h}}{\partial t} \Delta T}{\bar{h} + \hat{h}} \right) \right] \hat{\mathcal{H}} - \epsilon. \end{aligned} \quad (2)$$

Equation (2) includes MJO–MJO interactions as well as MJO–mean-state interactions. The heat flux forcing related to the MJO is estimated by first calculating the interaction between the full (mean plus MJO anomaly) heat flux and MLD, and then subtracting the mean from this total. We are only interested in entrainment that results from changes in MLD due to the MJO, so the entrainment term includes the effects of temporal variations in MLD at MJO time scales, with the mean (rectified) component removed. The rectified component was also estimated for the vertical and horizontal advection terms and found to be negligible, and so is excluded from Eq. (2). For each variable  $X$  we computed the seasonal and interannual signals ( $X_{seas}$  and  $X_{interann}$ ), then estimated the MJO signal to be  $\hat{X} = X - \bar{X} - X_{seas} - X_{interann}$ .

Spectral estimates of the  $\hat{X}$  component of each variable (not shown) revealed energy distributed broadly over the 20–100-day frequency band, with no single frequency standing out.

### b. Datasets

The terms in Eq. (2) that involve mixed layer temperature and depth and their derivatives were derived from Argo profile data, and the remaining terms came from gridded products, which are described in Table 1. The period of the MJO is roughly 50 days, so the eight phases of the Wheeler–Hendon MJO index are spaced, nominally, about 6 days apart. (Note that the MJO does not oscillate regularly, so these are rough temporal approximations.) Argo floats make temperature and salinity

TABLE 1. Gridded datasets and climatologies. “Temporal range” refers to the time range of the data product; note that for all products, we used available observations from 2004–10 in the present study.

Variable	Data source	Spatial resolution	Temporal resolution	Temporal range
SST	TMI	0.25° × 0.25°	1 day	1998–ongoing
Surface winds	CCMP	0.25° × 0.25°	6 h	1995–2009
OLR	NOAA	2.5° × 2.5°	1 day	1985–ongoing
Turbulent heat fluxes	OAFlux	1° × 1°	1 day	1985–ongoing
Sensible heat fluxes	ISCCP	1° × 1°	1 day	1985–2007
Surface currents	OSCAR	1/3° × 1/3°	5 day	1992–ongoing
Chlorophyll- <i>a</i>	NOBM	5/4° × 2/3°	5 day	1997–2006
Upper-ocean temperature and salinity	RG09	1° × 1°	1 month	2004–10

measurements of the top 1000–2000 m of the water column, with ∼5-m vertical resolution, approximately every 10 days, so numerous Argo profiles are needed in order to observe the temporal evolution of an MJO event. Although gridded Argo products have been developed (e.g., Roemmich and Gilson 2009, hereafter RG09), these generally have monthly temporal resolution, which is too coarse to capture the evolution of the MJO and would also smooth out some of the intraseasonal signal. We thus used the raw data from around 28 000 Argo profiles made within the domain of the tropical Indian and western Pacific Oceans (25°S–10°N, 55°E–180°) during the November–April months of 2004–10.

To illustrate the temporal resolution of Argo profiles, we compare mooring data from the Research Moored Array for African–Asian–Australian Monsoon Analysis and Prediction (RAMA) array (McPhaden et al. 2009) to nearby Argo observations (see the appendix and Fig. A1). Argo data offer an advantage over mooring observations in that they can be used to characterize subsurface variations over the entire spatial domain. Moreover, the vertical resolution of available mooring data [ $\geq$ 10-m depth spacing in the upper ocean for the RAMA–Tropical Atmosphere Ocean (TAO) arrays] is rather coarse for accurately resolving MLDs.

For each profile, the temperature measurement closest to the surface was used as a proxy for mixed layer temperature. To avoid erroneous mixed layer depth estimates, profiles with fewer than five measurements within the top 100 m of the water column were discarded, as were profiles without measurements in the top 6 m. MLD for each profile was taken to be the depth at which the density difference from a near-surface reference depth is equal to a threshold value  $\Delta\rho$ . A reference depth of 10 m is commonly used in MLD studies (e.g., de Boyer Montégut et al. 2004); however, in order to capture particularly shallow mixed layers that can form during the low-wind, clear-sky conditions of the suppressed MJO, we used a reference depth of 6 m. Qualitatively, our results were not sensitive to the choice of reference depth. By visually examining numerous profiles throughout the domain, we

determined that a density threshold of  $\Delta\rho = 0.05 \text{ kg m}^{-3}$  was most successfully able to capture the MLD. An example of MLD observations estimated from Argo and from a nearby mooring is shown in the appendix.

The heat flux components making up  $Q_{\text{net}}$  came from the objectively analyzed air–sea fluxes (OAFlux) and the International Satellite Cloud Climatology Project (ISCCP) products (Table 1). The OAFlux surface latent and sensible heat fluxes are based on satellite measurements and several reanalysis products (Yu and Weller 2007), and ISCCP surface shortwave and longwave radiation are derived using a radiative transfer model along with surface and atmospheric observations (Zhang et al. 2004). Kumar et al. (2011) compared several surface heat flux products with observations from Indian and Pacific Ocean moorings and found that the OAFlux and ISCCP products agree well with the observations of intraseasonal variability patterns. In section 5, we discuss the sensitivity of MJO heat budgets to the choice of flux product, and compare the OAFlux product with fluxes from the NCEP-2 reanalysis (Kanamitsu et al. 2002), the European Centre for Medium-Range Weather Forecasts (ECMWF) ERA-Interim reanalysis (ERA-I; Simmons et al. 2007), and the Japanese Ocean Flux datasets with Use of Remote sensing Observations (J-OFURO; Kubota et al. 2002).

The amount of incoming shortwave radiation entering the ocean mixed layer was estimated using an albedo of 7% (Morel and Antoine 1994). The  $Q_{\text{pen}}$  was estimated following Morel and Antoine (1994) and Sweeney et al. (2005) as

$$Q_{\text{pen}}(h) = 0.57 Q_{\text{sw}}(V_1 e^{-h/\zeta_1} + V_2 e^{-h/\zeta_2}), \quad (3)$$

where  $V_1$ ,  $V_2$ ,  $\zeta_1$ , and  $\zeta_2$  were estimated using chlorophyll-*a* observations from the National Aeronautics and Space Administration (NASA) Ocean Biogeochemical Model (NOBM), which is based on data assimilation of remotely sensed chlorophyll-*a* (Gregg 2008). Chlorophyll-*a* can vary at MJO time scales (Waliser et al. 2005; Vinayachandran and Saji 2008), so the MJO can modulate  $Q_{\text{pen}}$  through its

effects on both MLD and ocean chlorophyll. In addition, diurnal chlorophyll variations can modulate intraseasonal sea surface temperatures (Shinoda 2005). Unraveling these effects is beyond the scope of this study, particularly since Argo floats generally do not measure biological variables. We therefore evaluate Eq. (3) using seasonal-mean values of chlorophyll, so that  $Q_{\text{pen}}$  only varies spatially and with  $h$ .

The  $\mathbf{u}$  terms in Eq. (2) were estimated from the Ocean Surface Current Analyses (OSCAR) product, which is based on satellite winds and altimetric sea level anomaly data and consists of the total (geostrophic plus ageostrophic) zonal and meridional velocities at 10-m depth (Bonjean and Lagerloef 2002). We compared the OSCAR data to in situ surface current observations from the Triangle Trans-Ocean Buoy Network (TRITON)-TAO and RAMA mooring arrays and found that generally the in situ zonal currents are significantly correlated with the OSCAR product on MJO time scales, but the meridional currents tend to be less well correlated, particularly along the equator (cf. Johnson et al. 2007). Meridional surface currents at MJO time scales are generally weak ( $<0.03 \text{ m s}^{-1}$ ; Waliser et al. 2003), so this is not a large source of error in the overall analysis, although it may be locally important in some areas.

Ekman pumping,  $w_{\text{Ek}}$ , was estimated as  $\nabla \times (\boldsymbol{\tau}/f)\rho_s^{-1}$ , where  $\boldsymbol{\tau}$  is wind stress,  $\rho_s$  is the density of seawater, and  $f$  is the Coriolis frequency. Winds were obtained from the level 3.0 gridded cross-calibrated multiple platform (CCMP) wind vectors, which are derived from numerous satellite products (Ardizzone et al. 2009). Finally, we used outgoing longwave radiation (OLR) data as a proxy for tropical convective activity, relying on the National Oceanic and Atmospheric Administration (NOAA) product (Liebmann and Smith 1996). This is the same product that Wheeler and Hendon (2004) used to form the MJO index that the present study is based on. The gridded datasets have different spatial resolutions (Table 1), so each of the above fields was put on a common  $2.5^\circ \times 2.5^\circ$  grid ( $x_g, y_g$ ) using a  $2^\circ$  wide boxcar filter in each direction. With the exception of the OAFlux product, which is available only until 2007; the Quick Scatterometer (QuikSCAT) winds, which are available only until late 2009; and the NOBM chlorophyll-*a* product, which is available until 2006; we used observations from 2004 to 2010 for all datasets.

We estimated  $(T_{\text{seas}} + T_{\text{interann}})$  from the monthly gridded temperature dataset produced by RG09, which is based exclusively on Argo profiles and is available from 2004 onward. We also used density calculated from the RG09 gridded data to estimate the background MLD signal ( $h_{\text{seas}} + h_{\text{interann}}$ ). The mixed layer temperature and depth from RG09 were low-pass filtered with a 120-day cutoff, then projected onto the exact time

and position of each Argo profile using linear interpolation. This gave the expected background temperature and MLD component for each profile. To estimate the seasonal cycles of the variables derived from Argo ( $\partial T/\partial z, \Delta T$ ) as well as all of the gridded fields (Table 1), we fit annual and semiannual harmonics to the measurements in each grid box. For the gridded data we also used a 120-day lowpass filter to estimate the interannual signal. We did not explicitly estimate the interannual signal for the Argo variables  $\partial T/\partial z$  or  $\Delta T$ , as Argo profiles are irregularly distributed in time and space so low-pass filtering could have introduced biases. Generally, accurately estimating the seasonal and interannual signals proved to be the greatest limitation to resolving MJO variability: locations for which we could not successfully remove all of the background variability, for example the western Pacific Ocean, tended to yield poorer fits with large uncertainties.

### c. MJO heat budget composites

To estimate the terms in the MJO heat budget [Eq. (2)], we formed composites by averaging over numerous MJO events. The composites were defined using the Wheeler–Hendon MJO index (Wheeler and Hendon 2004), which is based on the first two empirical orthogonal functions of the combined fields of OLR and 200- and 850-hPa zonal winds averaged over  $15^\circ\text{S}$ – $15^\circ\text{N}$ . The index consists of a daily amplitude and phase, which is separated into eight discrete phases that represent the location of the active MJO. Although the MJO exhibits highly seasonal behavior due to the migration of the warmest SSTs, and thus convection, north and south of the equator (Zhang 2005), the Wheeler–Hendon index is independent of season. Thermodynamic anomalies associated with the MJO are strongest in boreal winter (Wheeler and Hendon 2004; Duvel and Vialard 2007), so we restricted our analysis to November–April. The mean oceanic and atmospheric conditions during this season are shown in Fig. 1.

At each grid point ( $x_g, y_g$ ), we formed composites of the individual variables in Eq. (2) by averaging over all measurements made during a given MJO phase. Only events for which the Wheeler–Hendon index had an amplitude greater than 1.5 were considered “significant” and were used in making the composites; the results were largely insensitive to the choice of this threshold, although a value outside of the amplitude range of 1–2 tended to degrade the composites. For the November–April time period, there were generally two significant events per year; for the 2004–10 period we averaged across around 11 events to obtain the composites. Note that the findings of this study were not sensitive to the number of events that we averaged over, nor the time span of the data used to

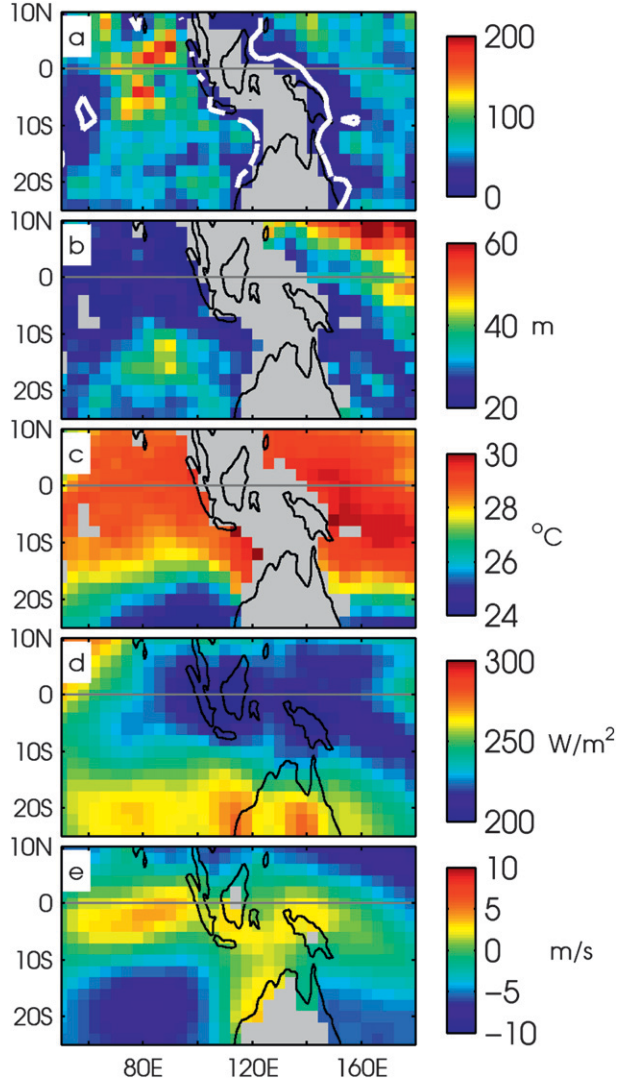


FIG. 1. (a) Average number of Argo profiles used to form the MJO composites presented in this study. (b)–(e) show boreal winter (November–April) means for (b) mixed layer depth, estimated from Argo observations; (c) mixed layer temperature estimated from Argo observations; (d) OLR, estimated from the NOAA dataset; and (e) zonal wind velocity, estimated from CCMP winds. The gray shading in (a) indicates where zero Argo profiles were available, and the white contour indicates that 20 profiles per grid box, per phase, were used to form the composites. In (b), (c), grid boxes with fewer than 20 profiles are masked out in gray.

form the composites, suggesting that our findings are robust despite interannual variations. Composites were formed from the gridded data by averaging across all of the observations made within  $\pm 2$  days of the significant MJO events. Compositing the Argo data was necessarily more involved as a result of the sparse and irregular temporal and spatial distribution of Argo profiles. To form statistically robust composites that captured the MJO spatial and temporal variability, it was necessary to

include Argo profiles from a time span and from grid boxes larger than those used for the gridded datasets. Instead of simply averaging the Argo data in each grid box, we fit a function to the observations and used it to extract information about the spatial and temporal patterns of MJO variability, including the MJO anomaly ( $\hat{T}, \hat{h}$ ) and the gradient terms ( $\partial T/\partial t, \partial T/\partial x, \partial T/\partial y$ , and  $\partial h/\partial t$ ). Details about this procedure and an example of regressions to mixed layer temperature and depth at one location are given in the appendix. Using grid boxes  $8^\circ$  wide in longitude and  $4^\circ$  wide in latitude, we found around 50–100 Argo profiles per grid box per phase that could be used for the regressions (Fig. 1a). The floats provide patchy spatial coverage in some regions, so we restrict our analysis to grid boxes where more than 20 Argo profiles were available for the regressions (white contour in Fig. 1a). This cutoff value was chosen empirically to eliminate grid boxes having too few data points to produce a sensible regression; within a reasonable range for a cutoff value (e.g., 10–50 profiles), our findings were not at all sensitive to the choice. No Argo floats have measured within the Indonesian archipelago, so the signal there could not be estimated in this study. In addition, the spatial coverage of Argo profiles is poor in the far western Pacific Ocean in comparison to the Indian Ocean, which made it more challenging to observe the MJO signal there.

We used the standard error of the composite average of each variable to represent its uncertainty. The uncertainties thus take into account the variation across different MJO events, which can be large, but not any systematic biases in the data. Errors in the satellite-derived quantities were generally small thanks to the great availability of data. In contrast, because Argo profiles are sparsely distributed in space and in time, there are large uncertainties in the quantities derived from these data. This is particularly evident in regions where there are few profiles (Fig. 1a).

### 3. Spatial patterns of MJO variability

#### a. MJO surface forcing

Not only is there great variation in the amplitude of individual MJO events, but the duration and structure of events are highly variable as well. It is important to keep in mind that the compositing procedure smooths out the variability of the MJO signal considerably. To highlight the significant patterns of variability, in all of the following figures the regions where the magnitude of the composite average is smaller than the standard error have been stippled. Thus, the nonstippled areas indicate a signal that is coherent with MJO forcing and is not merely noise. Figure 2 shows the progression of MJO atmospheric anomalies based on the Wheeler–Hendon

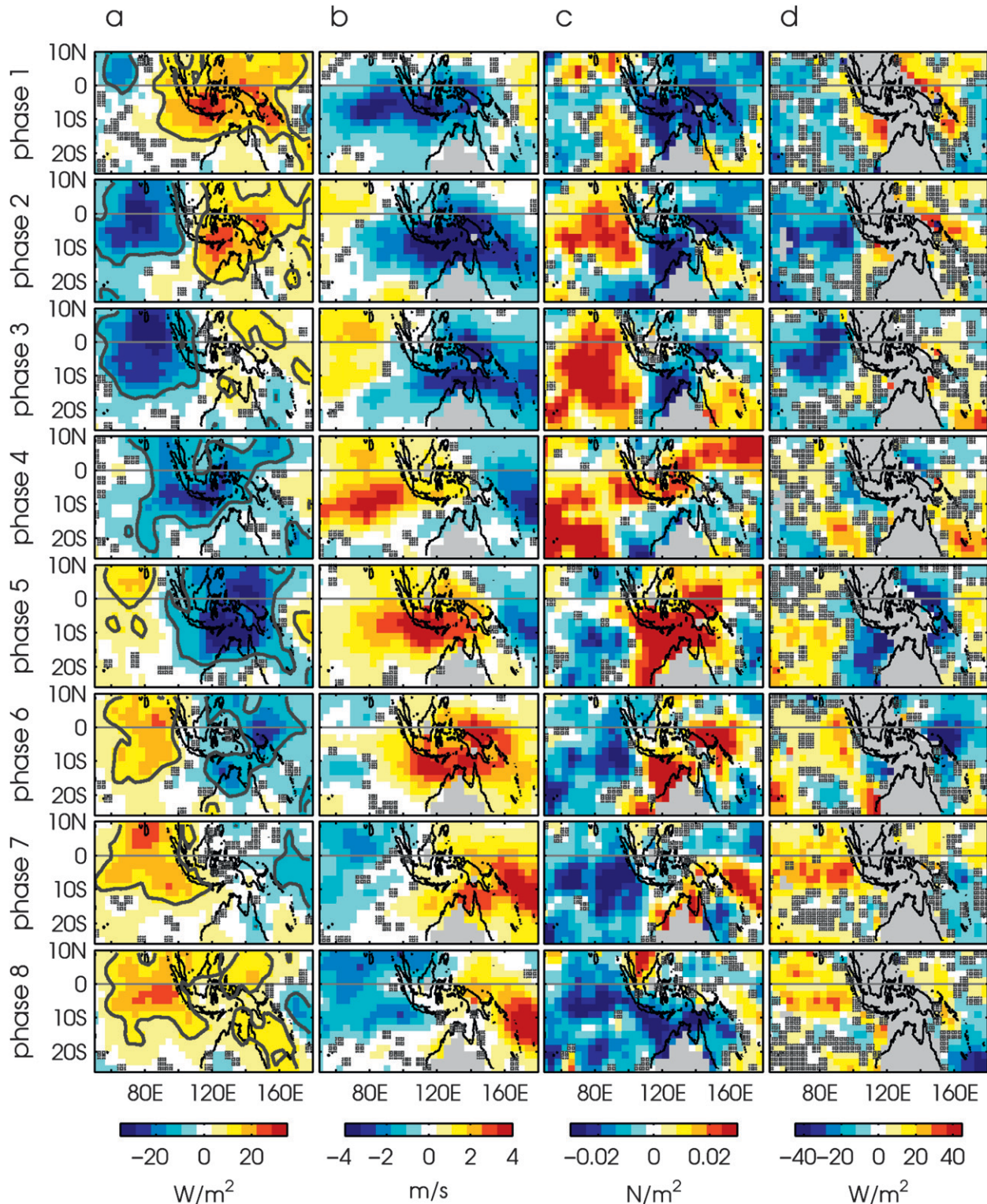


FIG. 2. Composites of November–April MJO anomalies based on the index of Wheeler and Hendon (2004): (a) OLR from NOAA data, (b) zonal wind speed from CCMP winds, (c) wind stress magnitude from CCMP winds, and (d)  $Q_o$  from the OAFlux product. Each column shows the progression of the MJO through each of the eight phases defined by the Wheeler–Hendon index. Regions where the magnitude of the composite value is less than the standard error are stippled. In (a)  $\text{OLR} = \pm 10 \text{ W m}^{-2}$  contours are shown; the regions where OLR anomalies exceed this threshold are considered to have significant MJO-related variability and are used in the subsequent analysis for estimating correlations and regressions between different fields.

MJO index (cf. Fig. 8 of Wheeler and Hendon 2004). For comparison, the mean (November–April) fields are shown in Figs. 1d,e. The signature of the MJO is seen clearly as eastward propagation of thick convective cells (negative OLR), flanked on both sides by clear skies (Fig. 2a). The active MJO signal is strongest over the central and eastern Indian Ocean in phases 3–4 (OLR anomalies  $< -20 \text{ W m}^{-2}$ ). In phases 5–6 the convective anomalies move eastward over the Indo-Pacific warm pool, then begin to weaken and move southward. By phases 7–8, the convective anomalies have reached the central Pacific Ocean and weakened considerably ( $\text{OLR} \sim -15 \text{ W m}^{-2}$ ); at the same time, the suppressed MJO conditions are strongest, with positive OLR anomalies ( $> 15 \text{ W m}^{-2}$ ) extending from the central Indian to the western Pacific Ocean. Interestingly, the spatial patterns of mean November–April OLR have a similar pattern to the MJO anomalies in OLR, with a thick band of low OLR that spans  $10^\circ\text{S}$ – $10^\circ\text{N}$  and stretches eastward from  $80^\circ\text{E}$  and into the western Pacific Ocean (Fig. 1d). This suggests that in a given phase, the discrepancy between regions experiencing active and suppressed conditions will be enhanced. The  $\text{OLR} \pm 10 \text{ W m}^{-2}$  contour is shown in order to highlight the regions where the MJO convective forcing is strongest and therefore the response of the upper ocean is expected to be large; correlations and regressions presented later in this study are restricted to grid boxes for which the OLR anomaly exceeds this value.

Zonal wind anomalies also show a systematic MJO signal: strong westerly wind anomalies ( $> 2 \text{ m s}^{-1}$ ) are associated with the active MJO, and slightly weaker easterly wind anomalies ( $-1.5 \text{ m s}^{-1}$ ) with the suppressed MJO (Fig. 2b). Note that the composite values shown in Fig. 2b represent averages; individual wind bursts can be much stronger [e.g.,  $8 \text{ m s}^{-1}$  westerly wind anomalies were reported by Cronin and McPhaden (2002) in the western Pacific Ocean]. To first order, net heat flux variations on MJO time scales are controlled by perturbations in the shortwave and latent heat flux caused, respectively, by variations in convection and winds (Woolnough et al. 2000). As a result, the phase relationship between convection and winds has important consequences for the patterns of net heat flux and thus the MJO mixed layer temperature trend. Zhang and McPhaden (2000) describe two models for MJO forcing. In model 1, maximum westerly winds lag (i.e., are to the west of) the peak convection, so there are two active forcing regimes: one beneath the peak westerlies, where latent heat loss and wind stirring are strong, and one beneath the convective center, where incoming solar heat flux is anomalously low. In model 2, the peak MJO westerlies and convection are collocated and there is a single forcing regime. Model 2

tends to cool (and heat) the ocean more efficiently, since the convection and winds act in phase. Hendon and Salby (1994) and Shinoda et al. (1998) found that the wind–convection phasing resembles model 1 in the equatorial Indian Ocean and model 2 in the western Pacific Ocean. Indeed, comparing Figs. 2a,b reveals that in the Indian Ocean anomalous OLR tends to lead anomalous zonal wind, whereas in the Pacific Ocean they are more closely aligned. However, variations in latent heat flux are controlled by anomalies in the magnitude of the wind stress (rather than the zonal wind), so it is necessary to consider the MJO anomalies in the context of the background wind field. Figure 1e shows that the boreal winter zonal winds are strongly westerly between  $10^\circ\text{S}$  and  $5^\circ\text{N}$  in the Indian and western Pacific Oceans as well as throughout the region between Indonesia and Australia, and easterly elsewhere in the domain, which means that zonal wind anomalies associated with the MJO will have different impacts on the ocean mixed layer in different regions. This can be understood by considering anomalous wind stress magnitude ( $|\hat{\tau}|$ ; Fig. 2c). The spatial patterns of  $|\hat{\tau}|$  have a coherent spatial signal at MJO time scales, but the propagation that characterizes the zonal wind and convective anomalies is less evident. While anomalous convection marches steadily eastward during the course of the MJO, the strongest anomalies in wind stress remain relatively stationary over the southwestern tropical Indian Ocean during phases 2–4, then over the region between northern Australia and Java during phases 5–7. In this region, MJO convective and wind anomalies are consistently out of phase with the rest of the Indian Ocean basin, and much more closely resemble conditions in the far western Pacific Ocean (e.g., the band of anomalous wind stress magnitude that can be seen just northeast of Papua New Guinea and the Solomon Islands and south of the equator; Fig. 2c), where forcing is also strong in phases 5–7. Furthermore, the band of wind stress magnitude northeast of Papua New Guinea is out of phase with wind stress elsewhere in the Pacific Ocean, so the response of the upper ocean to the MJO is not expected to be uniform throughout that basin. In summary, Fig. 2 illustrates that neither of the two models described by Zhang and McPhaden (2000) can easily explain the response of the upper ocean to MJO forcing.

The signature of the MJO is apparent in the corrected net heat flux,  $Q_o$  (Fig. 2d): large negative anomalies, indicating heat loss from the ocean surface, propagate eastward in concert with the active MJO, with maximum amplitudes ( $-25 \text{ W m}^{-2}$ ) in phases 4–5 over the equatorial Indo-Pacific region. The patterns generally resemble those of OLR (Fig. 2a), suggesting that they may be more strongly controlled by convective anomalies than by winds; however, in regions where OLR anomalies

are relatively weak, the role of anomalous MJO winds may be more important.

By the time the MJO atmospheric anomalies have reached the central Pacific Ocean, anomalous convection and winds have weakened considerably (Wheeler and Hendon 2004), and the processes governing mixed layer dynamics at MJO time scales are different than those in the Indian and western Pacific Oceans (Maloney and Kiehl 2002; McPhaden 2002; Lucas et al. 2010). For example, oceanic Kelvin waves are generated in the western Pacific Ocean by MJO-related wind bursts, then they propagate eastward along the equator where they affect the upper ocean in the eastern equatorial Pacific where there is no direct atmospheric forcing on MJO time scales (Kessler et al. 1995). In addition, advective processes are possible as a result of strong temperature gradients at the edge of the western Pacific warm pool (Fig. 1c; see Shinoda and Hendon 2001). Roughly around the date line, there appears to be a shift in the relative importance of one-dimensional versus dynamical processes on the MJO's mixed layer impacts (McPhaden 2002; Lucas et al. 2010). Thus, in the present study we limit our analysis to the Indian and Pacific Ocean west of the date line, where MJO surface forcing is large.

#### b. Mixed layer response to MJO forcing

The anomalous response of the mixed layer to MJO forcing is shown in Fig. 3. Composite MJO anomalies of MLD exhibit systematic variations, particularly in the Indian Ocean, with amplitudes of up to around  $\pm 10$  m (Fig. 3a). The spatial structures of MLD generally resemble those of wind stress and net heat flux (Figs. 2c,d), consistent with the model that diabatic cooling and wind stirring during the active MJO both contribute to mixed layer deepening, and surface warming and light winds during the suppressed MJO cause the mixed layer to shoal. The patterns of MLD variations are largely coherent over the Indian Ocean ( $10^{\circ}\text{S}$ – $10^{\circ}\text{N}$ ,  $60^{\circ}$ – $100^{\circ}\text{E}$ ) and the far western Pacific Ocean (west of  $160^{\circ}\text{E}$  and  $\pm 5^{\circ}$  of the equator). In the central Pacific Ocean there is no strong MJO signal in MLD. This may be because MJO convection and wind anomalies are not in phase over this region; or it may reflect the influence of other processes that affect MLD and are also modulated by the MJO, such as precipitation, horizontal ocean dynamics, or Ekman pumping.

Composite mixed layer temperature anomalies also display strong, systematic spatial and temporal patterns of MJO variability (Fig. 3b). Throughout the Indian Ocean, the mixed layer temperature patterns are similar to those of MLD (Fig. 3a), but with the opposite sign: mixed layers are anomalously cool during the active MJO and anomalously warm during the suppressed

MJO. Temperature anomalies lag heat flux anomalies (Fig. 2d) by around one phase, consistent with the model that heat flux anomalies drive the mixed layer temperature signal. Although the temperature signal is slightly weaker in the Pacific Ocean than in the Indian Ocean, it varies systematically at MJO time scales and is also consistent with being driven by net heat flux. The largest MJO temperature signal (peak-to-peak amplitude of around  $0.6^{\circ}\text{C}$ ) is seen in the northwestern Australian basin between Java and northern Australia, as has been observed previously (Duvel and Vialard 2007), where wind stress and heat flux anomalies are both strong (Figs. 2c,d). There are also strong variations in the Seychelles–Chagos thermocline ridge region (around  $5^{\circ}$ – $10^{\circ}\text{S}$ ,  $60^{\circ}$ – $90^{\circ}\text{E}$ ).

#### c. MJO heat budgets

To assess which processes contribute to the observed trends in mixed layer temperature, we formed composite maps of the individual terms in the heat budget [Eq. (2)]. These are shown in Fig. 4, with the exception of the vertical advection term, which is negligible (magnitude  $< 0.001^{\circ}\text{C day}^{-1}$ ) everywhere. It is evident from the large-scale patterns that the MJO mixed layer temperature trend (Fig. 4a) is driven by anomalies in corrected net heat flux (Fig. 4b), although the magnitude of the heat flux forcing term generally appears larger than that of  $\partial T/\partial t$ . Generally, horizontal advection is small ( $< 0.005^{\circ}\text{C day}^{-1}$ ) throughout the domain (Fig. 4c), though it can be as large as the local temperature tendency in the central Pacific Ocean east of around  $160^{\circ}\text{E}$ . There, strong anomalous wind bursts associated with the MJO excite zonal surface jets along the equator, which act on the mean temperature gradient (e.g., Fig. 1c) to advect heat zonally (e.g., Kessler et al. 1995).

Vertical entrainment associated with the MJO can be large, but the uncertainty in  $\partial h/\partial t$  is the same order as the signal itself, so entrainment is generally not statistically significant (Fig. 4d). However, widespread, significant entrainment cooling occurs in the central Indian Ocean during the onset of active MJO conditions in phase 1. There, both wind stirring and diabatic cooling appear to contribute to the rapid deepening of the mixed layer (up to  $1\text{ m day}^{-1}$ ), as can be inferred by comparing the phase 1 forcing patterns (Figs. 2c,d) with the phase 1–2 shift in the mixed layer response (Fig. 3). This basin-scale entrainment cooling increases the discrepancy between  $\partial T/\partial t$  and the corrected net heat flux forcing in phase 1 (Figs. 4a,b). Interestingly, entrainment cooling in the western Pacific Ocean is negligible despite the strong mixed layer deepening in phases 6–8 (Fig. 3a). This is because there is a persistent barrier layer in this region (Sprintall and McPhaden 1994; de Boyer

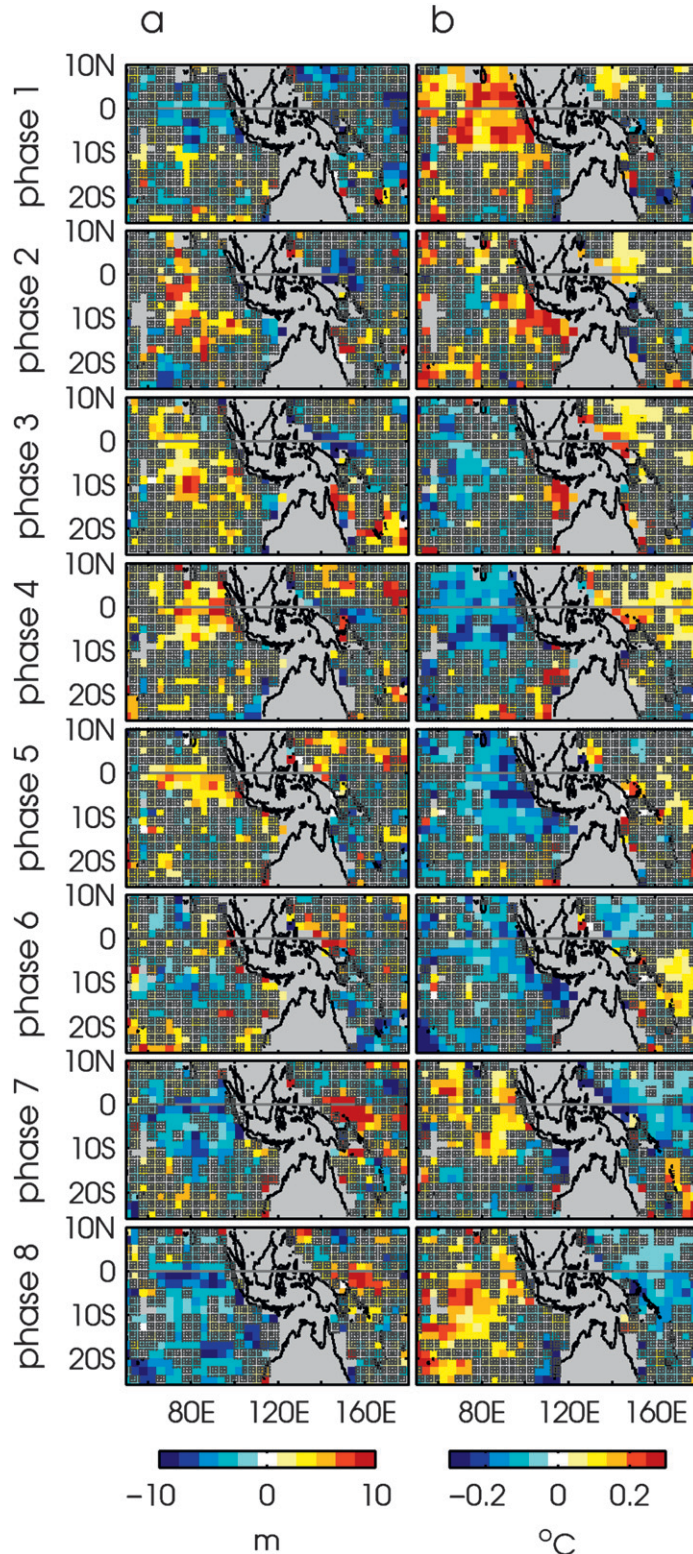


FIG. 3. Composites of November–April MJO anomalies based on the index of Wheeler and Hendon (2004) and data from Argo profiles: (a) mixed layer depth and (b) mixed layer temperature. Grid boxes where fewer than 20 profiles were available to compute the regressions have been masked out in gray; regions where the magnitude of the composite value is less than the standard error are stippled.

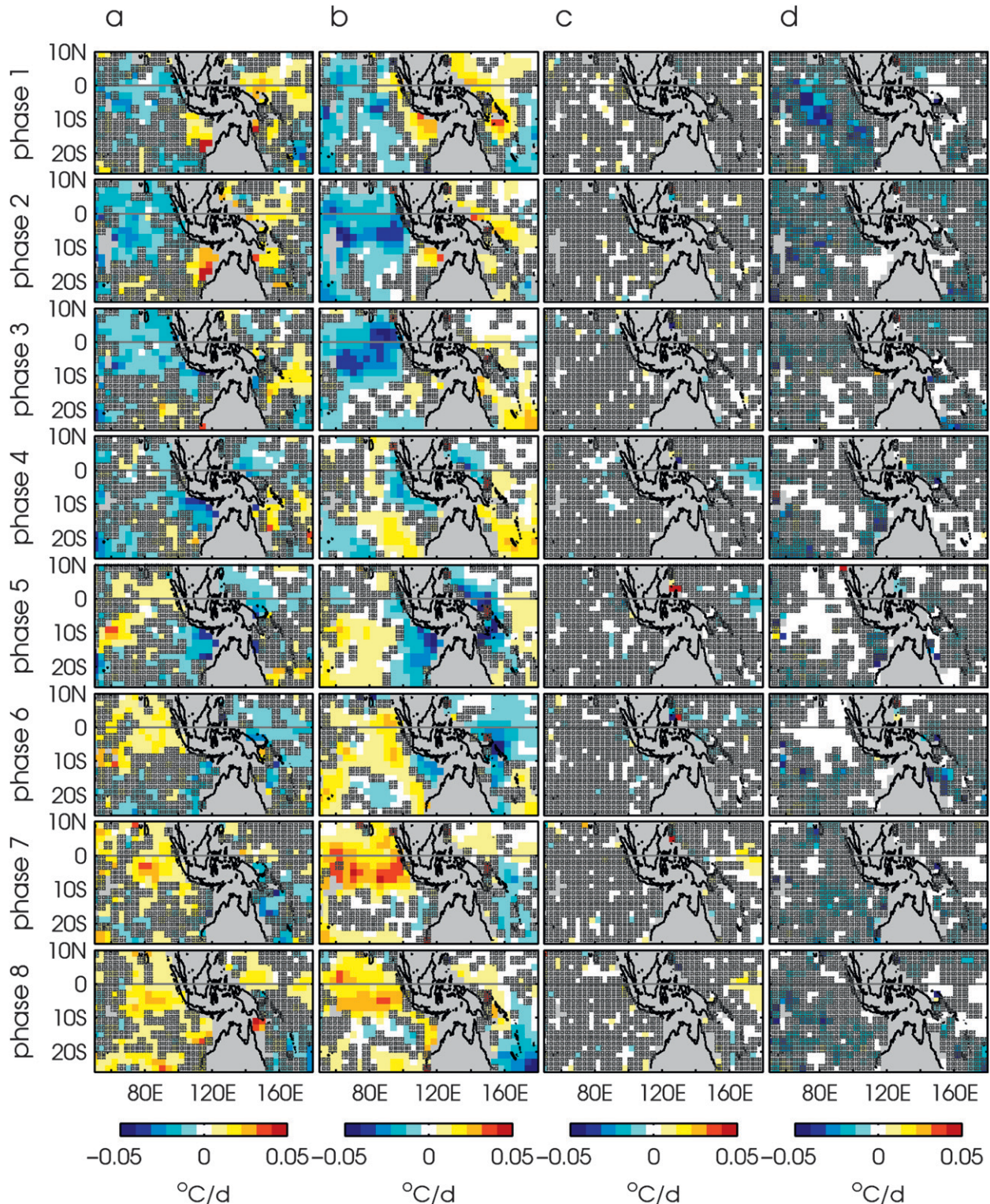


FIG. 4. Composites of November–April MJO heat budget terms: (a)  $\partial T/\partial t$ , (b) corrected net heat flux forcing, (c) horizontal advection, and (d) vertical entrainment. Positive values indicate mixed layer warming. MJO phases 1–8 are based on the Wheeler and Hendon (2004) index. Grid boxes where fewer than 20 Argo profiles were available have been masked out in gray; regions where the composite value is less than the standard error are stippled.

Montégut et al. 2007), which means that the water that gets entrained into the mixed layer is of a similar temperature as the mixed layer and thus does not produce cooling (e.g., Vialard and Delecluse 1998). Indeed, Argo-based estimates of the temperature jump at the base of the mixed layer,  $\Delta T$ , exceed  $1.5^{\circ}\text{C}$  throughout much of the Indo-Pacific domain, except in the western Pacific Ocean and west of Sumatra, where there are persistent barrier layers (e.g., de Boyer Montégut et al. 2007) and  $\Delta T$  is an order smaller (not shown). Also note that in individual profiles  $\Delta T$  can be negative, indicating a temperature inversion (which can arise from the presence of a barrier layer; cf. Anderson et al. 1996); however, in the composites  $\Delta T$  is positive everywhere and vertical entrainment always has a cooling effect. The role of the barrier layer in MJO dynamics, including how barrier-layer thickness varies on MJO time scales, will be addressed in a future study.

We quantify how the various terms in the heat budget (heat flux forcing, horizontal and vertical advection, and vertical entrainment) contribute to variations in the mixed layer temperature by estimating correlations ( $R^2$ ) and regression coefficients ( $\kappa$ , where an orthogonal linear regression was used because both the dependent and independent variables in the fits have observational errors) between  $\partial T/\partial t$  and each of these terms. It is evident from Fig. 4 that a given process may be more or less important depending on whether the MJO conditions are active or suppressed: for example, entrainment cooling only appears significant while the mixed layer is deepening during the active MJO. We therefore compute the statistics separately for active and suppressed MJO conditions by restricting the data points that are used in the comparisons: for the active MJO, we consider only the data points for which the composite anomalous wind stress magnitude ( $|\hat{\tau}|$ ) is positive and the composite OLR anomaly is less than  $-10 \text{ W m}^{-2}$ ; for the suppressed MJO we use points for which  $|\hat{\tau}| < 0$  and OLR  $> +10 \text{ W m}^{-2}$ . Note that the results of the statistical comparisons are not highly sensitive to the value of the OLR threshold. During both active and suppressed MJO conditions, corrected net heat flux forcing is significantly correlated with  $\partial T/\partial t$  ( $R^2 \sim 0.1$ ; Fig. 5a), though the regression analysis demonstrates that the magnitude of corrected net heat flux is 50%–80% larger than the magnitude of the temperature tendency ( $\kappa = 1.5$  during suppressed conditions and 1.8 during active conditions; Fig. 5b). The other terms in the heat budget do not compensate for this discrepancy, suggesting that either the heat flux forcing term is overestimated or the other terms in the heat budget are underestimated. Some possibilities for this are discussed in section 5. The regression coefficient between vertical entrainment and  $\partial T/\partial t$  is 0.5

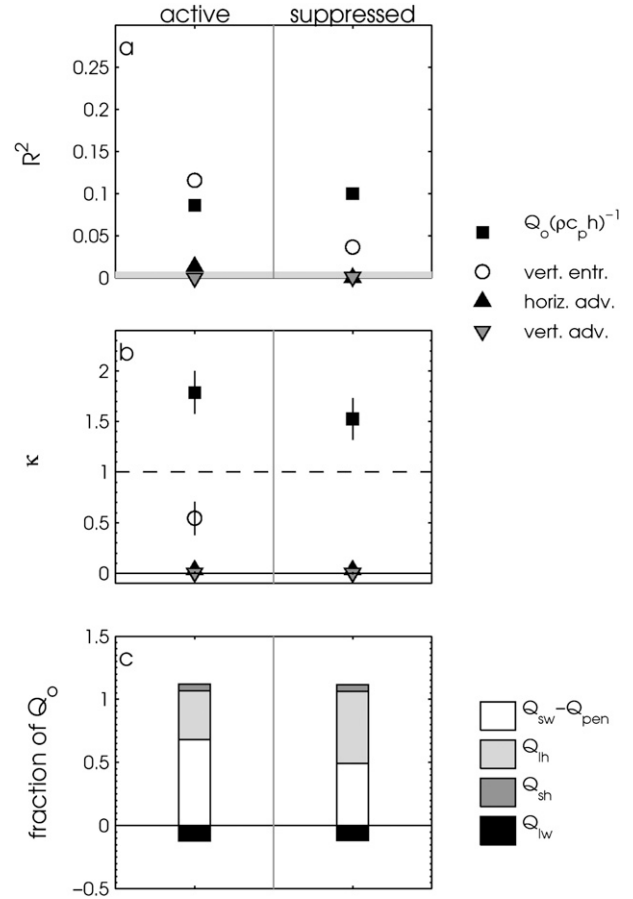


FIG. 5. (a) Correlation and (b) regression coefficient, between MJO composite anomalies of  $\partial T/\partial t$  and various terms in the heat budget [Eq. (2)]: corrected net heat flux forcing (squares), vertical entrainment (circles), horizontal advection (triangles), and vertical advection (inverted triangles). (c) The fraction of corrected net heat flux  $Q_o$  comprised by each flux component: corrected shortwave flux (white), latent heat flux (dark gray), longwave heat flux (light gray), and shortwave heat flux (black), estimated as the regression coefficient between the two terms. The data points used in each comparison have been limited based on the MJO anomalies of OLR and wind stress magnitude ( $|\hat{\tau}|$ ) in order to separately consider (left) active ( $|\hat{\tau}| < 0$  and anomalous OLR  $< -10 \text{ W m}^{-2}$ ) and (right) suppressed ( $|\hat{\tau}| < 0$  and anomalous OLR  $> +10 \text{ W m}^{-2}$ ) MJO conditions. In (a) the shading indicates the 95% significance level; in (b)  $\kappa = 1$  is indicated with a dashed line.

during the active MJO and zero during the suppressed MJO (Fig. 5b), which suggests that vertical entrainment causes up to half of the observed temperature variations during active MJO conditions, but does not impact mixed layer temperature during the suppressed MJO. Interestingly, the correlation between entrainment and mixed layer temperature tendency is also significant during suppressed conditions ( $R^2 = 0.04$ ; Fig. 5a), which indicates that although it does not contribute to the budget, vertical entrainment does covary with  $\partial T/\partial t$ . Similarly,

the correlation coefficients between  $\partial T/\partial t$  and both horizontal and vertical advection are weakly significant during the active MJO (Fig. 5a), demonstrating that although horizontal and vertical advection do not contribute statistically significant amounts to  $\partial T/\partial t$  (Fig. 5b), they vary systematically at MJO time scales.

By regressing  $Q_o$  against its constituent components, it is possible to assess which processes dominate the variations in corrected net heat flux forcing, and thus  $\partial T/\partial t$ , at MJO time scales (Fig. 5c). During active conditions, the shortwave heat flux (corrected for  $Q_{\text{pen}}$ ) comprises 70% of anomalous  $Q_o$ . The anomalous latent heat flux that results from wind stress anomalies is of secondary importance, accounting for around 40% of the corrected net heat flux. This demonstrates that anomalous convection is the primary driver of mixed layer cooling during active MJO conditions. During the suppressed phase, corrected shortwave flux and latent heat flux each account for around 55% of the  $Q_o$  anomaly, suggesting that warming resulting from the anomalous low-wind conditions is as important as anomalous heating. In both active and suppressed MJO conditions, longwave fluxes represent around -15% of  $Q_o$ ; that this fraction is negative means that longwave fluxes act in the opposite direction of the net heat flux. For example, the anomaly in outgoing longwave radiation caused by cloudy conditions during the active MJO acts to warm the mixed layer. Sensible fluxes account for less than 5% of  $Q_o$ .

#### 4. Implications of MLD variations associated with the MJO

Historically, MJO variations in MLD have been difficult to estimate explicitly, so their impacts on the heat budget have only been considered indirectly. For example, Jayakumar et al. (2011) used a MJO mixed layer heat budget analysis of the central Indian Ocean to show that the correlation between  $\partial T/\partial t$  and corrected net heat flux forcing was similar whether a fixed or a variable MLD was used in the calculation. Similarly, Duvel et al. (2004) found that even when climatological MLD is used, there is good agreement between  $\partial T/\partial t$  and corrected net heat flux forcing, and concluded that intra-seasonal variations in MLD are of secondary importance in the heat budget. However, Shinoda and Hendon (1998) used a one-dimensional mixed layer model to show that MJO variations in MLD can substantially affect the mixed layer heat content of the western Pacific Ocean by way of two mechanisms. First, since the net corrected heat flux anomaly is scaled by MLD [i.e.,  $h$  appears in the denominator of term  $a$  in Eq. (1)], variations in MLD can modulate the heat flux forcing ("scaling effect"); and second, variations in

MLD can affect  $Q_{\text{pen}}$ , the amount of incoming solar heat flux lost through the base of the mixed layer [Eq. (3); "penetrative effect"]. We quantify how these two mechanisms can individually modulate the corrected net heat flux forcing term [ $Q_{\text{net}} - Q_{\text{pen}}(h)(\rho c_p h)^{-1}$ : the scaling effect is estimated by using both the seasonal-mean MLD ( $h = \bar{h}$ ) and the observed seasonal-mean plus MJO-varying MLD ( $h = \bar{h} + \hat{h}$ ) in the denominator of this term, and the penetrative effect is estimated by comparing  $h = \bar{h}$  and  $h = \bar{h} + \hat{h}$  in the  $Q_{\text{pen}}$  part of this term. As noted by Shinoda and Hendon (1998), negative net heat fluxes are associated with deep mixed layers and positive heat fluxes with shallow mixed layers (Figs. 2d and 3a), so the scaling effect nearly always results in a warming pattern; that is, when  $h = \bar{h} + \hat{h}$  is used in the denominator of the corrected net heat flux forcing term, the term is more positive (Fig. 6a). The scaling effect is significant in the central equatorial Indian Ocean during both the peak active and suppressed MJO (phases 2–3 and 8), where it has a magnitude of around  $0.003^{\circ}\text{--}0.008^{\circ}\text{C day}^{-1}$ . The scaling effect can also be seen just west of Sumatra when MJO conditions there are active (phases 4–5).

During the active MJO, mixed layers are deeper so less incoming radiation is lost through the base of the mixed layer, thus the penetrative effect is positive [i.e.,  $Q_{\text{pen}}(\bar{h} + \hat{h})$  is warmer than  $Q_{\text{pen}}(\bar{h})$ ]; similarly, shallow mixed layers that occur during the suppressed MJO allow more of the incoming heat to pass through the mixed layer, so the penetrative effect is negative (Fig. 6b). Further complicating matters, the combination of a thin mixed layer and a large  $Q_{\text{pen}}$  during suppressed MJO conditions can cause the water below the mixed layer to warm. When the mixed layer deepens during the subsequent active phase, this heat can be rereleased into the mixed layer. In other words, it is possible for entrainment at the base of the mixed layer to increase mixed layer temperature (Shinoda and Hendon 1998). We build this effect into our heat budget by using Argo data to estimate  $\Delta T$ , the difference in temperature between the water within and 10 m below the mixed layer. However, this estimate of  $\Delta T$  may not accurately represent the temperature of the water that gets entrained into the mixed layer, for example  $Q_{\text{pen}}$  only heats a very thin layer beneath the mixed layer base, so we are unable to quantify the effect of MLD variations on entrainment heat flux. It is expected that using a variable MLD would reduce entrainment cooling during active conditions, thereby producing a warmer mixed layer, in regions with shallow mixed layers and large  $Q_{\text{pen}}$ . For example, there would be a positive temperature anomaly in the Indian Ocean when the mixed layer deepens in phases 2–3, enhancing the positive penetrative effect (Fig. 6a). The penetrative

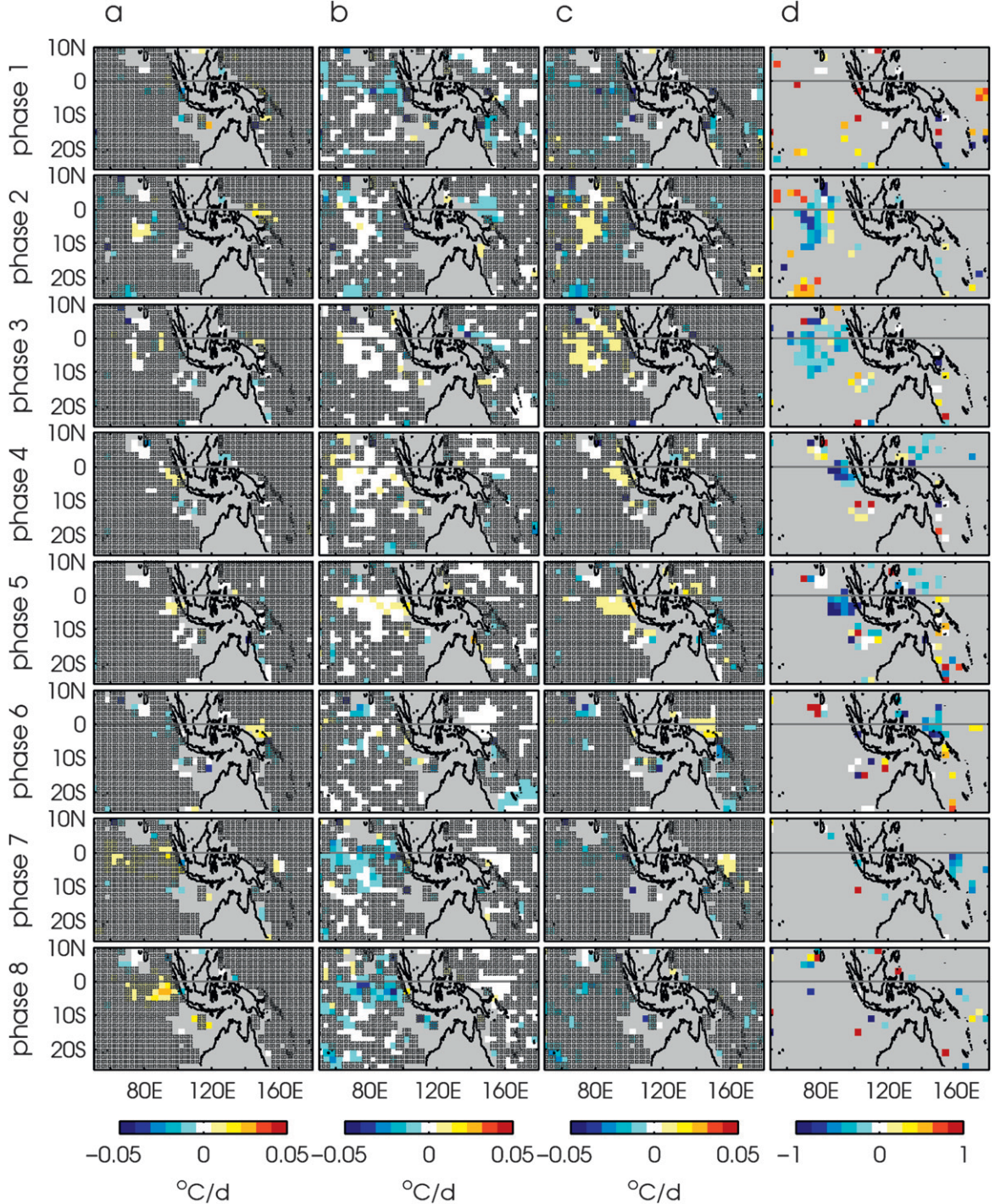


FIG. 6. Composites illustrating the effect of MJO anomalies in MLD on mixed layer heat forcing, estimated by calculating  $Q_o(\rho c_p h)^{-1}$  using both  $h = \bar{h}$  and  $h = \bar{h} + \hat{h}$  and then computing the difference: (a) scaling effect, comparing  $h$  in the denominator; (b) penetrative effect, comparing  $h$  in the  $Q_{\text{pen}}$  term; and (c) sum of (a) and (b), representing the net effect of MJO-related MLD variations on the mixed layer heat budget. Positive values indicate that MLD variations due to the MJO produce a warmer mixed layer in comparison to a fixed MLD. Grid boxes where fewer than 20 Argo profiles were available have been masked out in gray; regions where the composite value is less than the standard error are stippled. The color scaling is the same as used in the plots of the heat budget terms (Fig. 4). (d) Fraction of the corrected net heat flux forcing (Fig. 4b) represented by (c), with negative values indicating that using a mean MLD in the heat budget overestimates the corrected net heat flux, and positive values indicating an underestimate. For clarity, all grid boxes where the composite error is less than the standard error have been masked in gray.

effect is strong ( $\pm 0.03^{\circ}\text{C day}^{-1}$ ) throughout the central Indian and far western Pacific Oceans, where MLD variations are large (Fig. 3a).

Both the scaling and penetrative effects have the same sign during the active MJO, so using the MJO-varying MLD results in a corrected net heat flux forcing up to  $0.008^{\circ}\text{C day}^{-1}$  warmer than using a fixed MLD (phases 2–3 in the central Indian Ocean and phases 4–4 west of Sumatra; Fig. 6c). In comparison, the corrected net heat flux forcing term used in the heat budget during these phases has a value of around  $-0.02^{\circ}\text{C}$  (Fig. 4b), so the combined scaling and penetrative effects represent about 40% of the corrected net heat flux forcing (Fig. 6d). In other words, using a fixed MLD to estimate  $\partial T/\partial t$  based on observed  $Q_o$  would overestimate the signal by  $\sim 40\%$  during the active MJO.

In contrast to the active MJO, the scaling and penetrative effects essentially cancel each other out during the suppressed MJO, and the net effect is not statistically significant (Figs. 6c,d).

In this study we have estimated  $Q_{\text{pen}}$  using seasonal-mean chlorophyll [Eq. (3)]. However, ocean chlorophyll concentration can vary at MJO time scales (Waliser et al. 2005; Vinayachandran and Saji 2008; Resplandy et al. 2009): the active MJO is associated with an increase in chlorophyll, which tends to decrease  $Q_{\text{pen}}$  [Eq. (3)]. We estimated this effect by forming MJO composites of the NOBM chlorophyll-*a* product (Gregg 2008) and calculating the resulting change in  $Q_{\text{pen}}$ . In the active phase, MJO chlorophyll variations reduce  $Q_{\text{pen}}$  by a maximum of around 5%, and in the suppressed phase they increase  $Q_{\text{pen}}$  by less than 5% (not shown). Since  $Q_{\text{pen}}$  has around a 10%–20% impact on the net heat flux forcing, we conclude that the effects of MJO-related chlorophyll variations on the heat budget are relatively unimportant. On the other hand, diurnal chlorophyll variations can significantly impact the temperature of the mixed layer on intraseasonal time scales through modulation of  $Q_{\text{pen}}$  (Shinoda 2005); this effect is not considered in the present study, and may contribute to the uncertainty in the heat budget.

## 5. Sensitivities and uncertainties

### a. Uncertainties in heat budget terms

The residual of the heat budget [ $\epsilon$  in Eq. (2); Fig. 7a] is generally on the same order as the mixed layer temperature tendency itself (Fig. 4a), suggesting that the approach used in this study does not allow all of the upper-ocean processes associated with the MJO to be precisely quantified. This is unsurprising: there are many feedbacks and scale interactions, and the atmospheric

forcing can vary from one event to the next, so mixed layer temperature variations at MJO time scales are not expected to respond perfectly linearly to MJO forcing. The goal of this study was not to close the heat budget, but rather to examine the dynamical processes that contribute to mixed layer temperature variations on MJO time scales, so it is enlightening to explore some of the potential sources of error in the heat budget estimates.

Generally, the amplitude of the anomalous corrected net heat flux forcing is around 50%–80% larger than the observed temperature tendency (Fig. 5b). One possibility is that because  $\partial T/\partial t$  is estimated using the relatively sparse set of Argo profile data, the variance is underestimated in comparison to that of the heat flux composites, which are based on many more data points. We tested this by comparing  $\partial T/\partial t$  estimated from Argo with  $\partial T/\partial t$  estimated from the gridded, satellite-derived SST data from the Tropical Rainfall Measuring Mission (TRMM) Microwave Imager (TMI), and found that both methods yield results with similar variance (see the appendix). Moreover, a regression analysis using the TMI-derived values of  $\partial T/\partial t$  revealed that the corrected net heat flux forcing is 1.3–1.7 times as large as the temperature tendency (cf. 1.4 estimated using Argo-derived  $\partial T/\partial t$ ; Fig. 5b), suggesting that the use of mixed layer temperatures from Argo does not systematically degrade the heat budget.

The composite averages do not take diurnal variability into account. Since Argo profiles sample the mixed layer at random times of day, measurements of mixed layer temperature and depth may be noisy in regions where diurnal variations are large (e.g., between northern Australia and Java and in the western Pacific warm pool; Bellenger and Duvel 2009), which may degrade the heat budgets there. Convection and winds affect the ability of the upper ocean to form diurnal warm layers, so the MJO itself may modulate the amplitude of the diurnal signal, further complicating the picture (Bellenger and Duvel 2009). The interplay between diurnal and intraseasonal variations is emerging as a potentially important mechanism in MJO dynamics (Shinoda and Hendon 1998; Bernie et al. 2005; Shinoda 2005; Woolnough et al. 2007; Bernie et al. 2008), but Argo floats do not sample with sufficient vertical resolution or at shallow enough depths to adequately resolve the diurnal signal, so we do not attempt to unravel these processes in the present study.

The heat budget is considered to be closed where the magnitude of the residual is smaller than the error. The total error for the heat budget is so large that over most of the domain the heat budget is, in fact, closed (Fig. 7b); we now consider the sources of that error. The uncertainty of the vertical entrainment term is generally larger than the signal itself (Fig. 4d) as a result of large

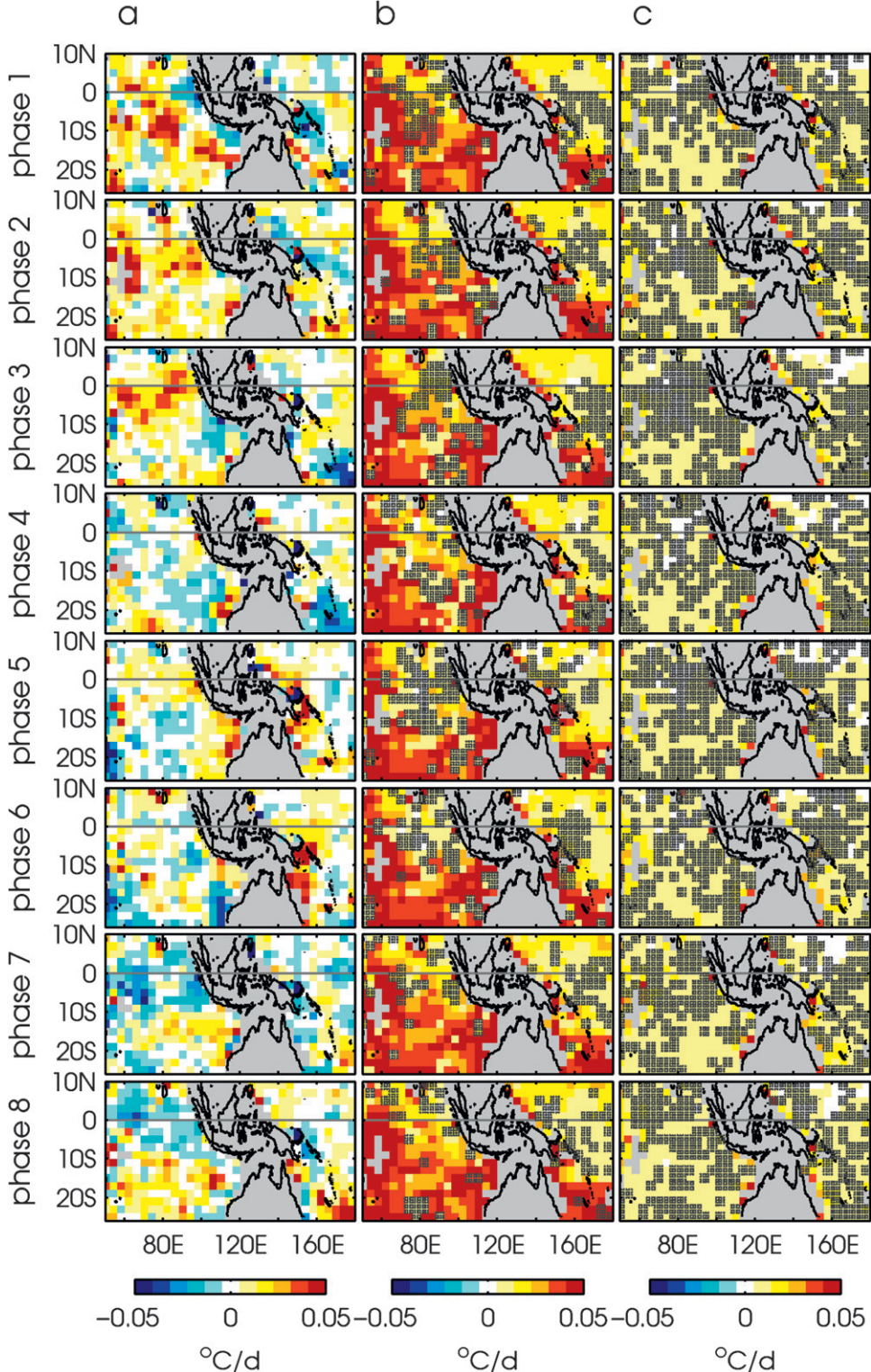


FIG. 7. Uncertainties associated with the composite November–April MJO heat budget: (a) residual ( $\epsilon$ ) and (b) error map for all terms in the MJO heat budget apart from  $\epsilon$  [ $\partial T/\partial t$ , heat flux forcing, horizontal and vertical advection, and entrainment; Eq. (2)]. The heat budget is considered to be “closed” when the amplitude of the residual is smaller than this term. (c) As in (b), but excluding the errors from vertical entrainment. In (b) and (c), regions where the budgets are not closed, based on the error map shown, are stippled. MJO phases 1–8 are based on the Wheeler and Hendon (2004) index. Grid boxes where fewer than 20 Argo profiles were available have been masked out in gray.

errors in the estimate of  $\partial h/\partial t$  from the Argo profile data. Interestingly, errors in the MJO signal in MLD are generally small (Fig. 3a), suggesting that the behavior of MLD is robust over different MJO events (e.g., the mixed layer systematically deepens during active conditions), but the *rate* at which the mixed layer deepens and shoals varies from event to event, so the  $\partial h/\partial t$  signal is noisy. We also note that  $\Delta T$  is estimated as the difference in temperature at the depth of the mixed layer and 10 m below. Though this term has a relatively low standard error, it may not accurately represent the temperature of water that gets entrained into the mixed layer, further increasing the uncertainty in the entrainment term. If the entrainment term is removed from the budget entirely, the total uncertainty in the heat budget estimate is substantially lower, and as a result the magnitude of the residual generally exceeds the uncertainty and the budget is not closed (e.g., large-scale stippling in Fig. 7c, which indicates that the heat budget is not closed). Thus, it is only because of the large uncertainties in entrainment that the heat budget can be closed (Fig. 7b).

There may also be large errors on the horizontal advection terms. The strength of horizontal advection depends on the location of surface current anomalies relative to the mixed layer temperature gradient, which can vary interannually (e.g., in the western Pacific Ocean due to ENSO), so averaging reduces the signal considerably. Also, as noted in section 2b, estimates of meridional currents from OSCAR may not be accurate. However, since the advection terms are generally small (Fig. 4c), it seems unlikely that errors in these terms are large enough to contribute a significant amount to the heat budget residual.

Finally, inaccuracies in how MLD is estimated could introduce a bias into the scaling of the corrected net heat flux term,  $Q_o(\rho c_p h)^{-1}$ . Defining MLD using a larger value of  $\Delta\rho$  produces systematically deeper mixed layers, and therefore a smaller net heat flux forcing term. However, we determined empirically that using a larger value of  $\Delta\rho$  tends to identify unrealistically deep mixed layers in comparison to the  $\Delta\rho = 0.05 \text{ kg m}^{-3}$  used in this study (section 2b). We therefore rule out the choice of  $\Delta\rho$  as an important source of error in the heat budget.

### b. Comparison of heat flux products

Heat flux is notoriously difficult to estimate accurately, and the various model reanalysis and observations-based products in general suffer from a lack of validation (Kumar et al. 2011). We evaluate the uncertainty in the heat flux term of the heat budget by computing MJO composites of  $Q_o$  using the NCEP-2 reanalysis, ECMWF ERA-I reanalysis, and J-OFURO product, along with the OAFlux product that was used for the

TABLE 2. Comparison of corrected net heat flux forcing and mixed layer temperature tendency for different heat flux products. Computations have been made using MJO composite observations from all grid points where the magnitude of the OLR anomaly exceeds  $10 \text{ W m}^{-2}$  (Fig. 2a). Relative variance is computed as the variance of the corrected net heat flux forcing divided by the variance of  $\partial T/\partial t$ . The 95% significance level for the correlations is  $R^2 = 0.010$ . The regression coefficient,  $\kappa$ , is computed using orthogonal linear regression as  $(Q_{\text{net}} - Q_{\text{pen}})(\rho c_p h)^{-1} = \kappa \partial T/\partial t$ . RMSD stands for root-mean-square difference.

	Relative variance ( $^{\circ}\text{C day}^{-1}$ )	$R^2$	$\kappa$	RMSD ( $^{\circ}\text{C day}^{-1}$ )
OAFlux	1.8	0.35	1.6	0.013
J-OFURO	2.0	0.26	1.9	0.015
ERA-I	2.1	0.25	1.9	0.015
NCEP-2	1.7	0.15	2.0	0.016

heat budget. All products yield the same qualitative patterns (e.g., Figs. 2d and 4b), but quantitatively they vary (Table 2). Since the advection and entrainment terms in the heat budget are generally small compared with the mixed layer temperature tendency (Fig. 5b), it is reasonable to evaluate the performance of each heat flux product by comparing  $Q_o(\rho c_p h)^{-1}$  to  $\partial T/\partial t$ . This comparison was made using several statistical tests: relative variance indicates how well the flux product captures the energy of the  $\partial T/\partial t$  signal; correlation ( $R^2$ ) describes how well the flux product captures the spatial and temporal variations of the signal; regression coefficient indicates how much the heat flux forcing overestimates the temperature tendency; and the root-mean-square difference (RMSD) quantifies the degree to which the signals differ. These analyses were performed using all data points for which the magnitude of the OLR anomaly exceeded  $10 \text{ W m}^{-2}$ : this does not differentiate between active and suppressed MJO conditions (cf. Fig. 5), but restricts the comparisons to data points for which MJO forcing is strong and so the composites are expected to represent MJO-related variability well. (Note that the comparisons were not sensitive to the choice of this threshold for OLR). For all products, correlations between  $Q_o(\rho c_p h)^{-1}$  and MJO temperature tendency are low but significant (Table 2). Overall, the OAFlux product performs best among the four products, with the largest correlation and smallest RMSD value and regression coefficient, and only a 60% overestimate of the variance in comparison to  $\partial T/\partial t$ . Although the relative variance of the NCEP-2 product is closest to unity compared to the other products, the correlation coefficient is particularly low and the RMSD is large, suggesting that NCEP-2 captures the energy, but not the signal, of the MJO. J-OFURO and ERA-I perform similarly, both overestimating the variance of  $\partial T/\partial t$  by a factor of 2 and overestimating the amplitude of

the signal by 90% (Table 2). These findings are consistent with the study by Kumar et al. (2011), who compared numerous heat flux products in the Seychelles–Chagos thermocline ridge region. That OAFlux performs best relative to the observations is unsurprising given that the ISCCP shortwave radiation used in OAFlux is based on satellite observations, whereas the shortwave fluxes used in NCEP-2 and ERA-I are based on models.

The small uncertainty in the corrected net heat flux term used in the budget (Fig. 4b) reflects only variability across multiple events and does not take systematic biases into account. Perhaps a more accurate method is to first estimate the composite  $Q_o$  from each heat flux product (Table 2), then use the standard deviation across the different products to represent the uncertainty. When this is done, the error maps for  $Q_o$  are on the same order as those on  $\partial T/\partial t$ , but the budget can generally still not be closed within the estimated uncertainty. This illustrates that heat flux is one of the largest sources of uncertainty in the MJO heat budget.

## 6. Summary

Composites of mixed layer temperature, depth, and heat budget terms (Figs. 3 and 4) have provided insight into how various dynamical and thermodynamical processes affect the mixed layer of the tropical Indian and western Pacific Oceans on MJO time scales. Although previous studies have addressed similar questions, the present study is novel in that it is the first to use in situ mixed layer observations to estimate a MJO mixed layer heat balance throughout the domain. We have shown that during the boreal winter (November–April), the MJO excites coherent variations in mixed layer depth and temperature throughout the Indian and western Pacific Oceans, with peak-to-peak composite amplitudes of more than 15 m and 0.6°C, respectively (Fig. 3). MJO variations in mixed layer depth are largest in the central Indian Ocean and the western Pacific Ocean, and mixed layer temperature anomalies are largest in the northwestern Australian basin (between Java and Australia) and the Seychelles–Chagos thermocline ridge (around 5°–10°S, 60°–90°E) regions (Fig. 3). Our observations are generally consistent with the model that the mixed layer deepens and cools during the active, cloudy-windy phase of the MJO, and shoals and warms during the clear-sky, low-wind conditions of the suppressed phase. This is particularly evident throughout the Indian Ocean, where anomalies in wind stress and net heat flux are nearly in phase and vary systematically throughout the life cycle of the MJO (Figs. 2c,d). The signals are similarly strong in the far western Pacific Ocean (west of 160°E and within

±5° of the equator). In contrast, the mixed layer temperature and depth anomalies in the central Pacific Ocean do not vary systematically at MJO time scales, likely because MJO wind and convective forcing over that region are not in phase.

A mixed layer heat budget analysis showed that large-scale patterns in mixed layer temperature tendency are governed by different processes during active and suppressed conditions. During the suppressed phase of the MJO, variations in shortwave and latent heat flux resulting from anomalously clear and calm conditions, respectively, contribute roughly equally to mixed layer warming. In the active MJO phase, shortwave radiation dominates the anomalous heat flux (70%) whereas latent heat flux accounts for only around 40%, suggesting that the relative role of winds and convection is asymmetrical between active and suppressed conditions. During active MJO conditions, entrainment cooling that results from mixed layer deepening represents around half of the observed  $\partial T/\partial t$  signal (Fig. 5b). This is seen most clearly throughout the central Indian Ocean, when there is an abrupt shift from suppressed to active MJO conditions in phases 1–2 and vertical entrainment cooling dominates the mixed layer temperature tendency (Fig. 4d). This finding may help to resolve the discrepancy between previous studies that examined intraseasonal variations in the heat content of the central Indian Ocean: Han et al. (2007) found that latent heat flux and vertical entrainment control SST changes on MJO time scales, whereas other authors have shown that heat flux variations alone, in particular shortwave radiation, dominate SST variations at MJO time scales (e.g., Duvel et al. 2004; Saji et al. 2006; Duvel and Vialard 2007; Vialard et al. 2008; Jayakumar et al. 2011). Our results suggest that net heat flux anomalies, dominate the overall heat budget, but entrainment cooling is important during the active MJO.

Horizontal and vertical advection of heat flux, though significantly correlated with the mixed layer temperature tendency during active MJO conditions (Fig. 5a), represent a negligible fraction of  $\partial T/\partial t$  (Fig. 5b), indicating that though these processes can be systematically excited by MJO forcing, their contribution to mixed layer temperature variations is not important in comparison to heat flux and vertical entrainment anomalies. However, we emphasize that the composites describe the average MJO, and thus do not preclude certain processes becoming important during individual events. The horizontal advection term, which at MJO time scales is primarily due to anomalous currents acting on the mean temperature gradient, only becomes significant east of around 160°E (Fig. 4c). This confirms that as the active MJO moves east over the Pacific Ocean, there is a shift

from direct atmospheric forcing of the mixed layer to indirect forcing via anomalous surface currents and equatorial waves (e.g., Lucas et al. 2010).

Corrected net heat flux forcing is around 40% larger than the  $\partial T/\partial t$  signal, suggesting that the heat flux forcing is overestimated or that other processes are underestimated. A discussion of potential error sources concludes that the large heat budget residual is likely due to a combination of factors. However, while the composite analysis is useful for assessing which processes are important in different locations and during different MJO conditions, there is enormous variability across MJO events that gets smoothed by the averaging. This means that it is likely that using a composite approach can only result in a closed mixed layer heat budget with a generous uncertainty budget (Fig. 7b).

This study revealed that MLD variations on MJO time scales modulate the heat budget by ~40% in the equatorial Indian and far western Pacific Oceans during active MJO conditions (Fig. 6d). In other words, using a “slab” mixed layer whose depth does not vary with the MJO can result in large overestimations of the mixed layer temperature changes forced by the MJO in these regions. This has potentially important consequences for how models simulate MJO anomalies in temperature, and thus air-sea interactions. Though there remains much debate over the importance of the role of the upper ocean in simulating the MJO, it is useful to understand where and to what extent MLD variations could impact the upper-ocean heat budget on MJO time scales.

Finally, we showed that the choice of heat flux product can radically affect the mixed layer heat budget, illustrating that in order to correctly estimate mixed layer temperature variations on intraseasonal time scales, developing and validating more accurate heat flux products should be a priority.

**Acknowledgments.** We gratefully acknowledge the many sources of data that made this study possible. The Argo data were collected and made freely available by the International Argo Project and the national programs that contribute to it (<http://www.argo.ucsd.edu>, <http://argo.jcommops.org>). Heat fluxes were obtained from Woods Hole Oceanographic Institution (OAFlux); ISCCP; NOAA/OAR/ESRL PSD, Boulder, Colorado (OLR and NCEP-2 reanalysis); ECMWF (ERA-I reanalysis); and the School of Marine Science and Technology, Tokai University (J-OFURO). The OSCAR data were obtained from the NASA Jet Propulsion Laboratory’s Physical Oceanography DAAC and developed by Earth and Space Research. Chlorophyll-*a* data are available from the Giovanni online data system, which is developed and maintained by the NASA

Goddard Earth Sciences Data and Information Services Center. TMI SST data are produced by Remote Sensing Systems and sponsored by the NASA Earth Science MEaSUREs DISCOVER Project and are available online (<http://www.remss.com>). Wind data were provided by the Global Modeling and Assimilation Office at the NASA Goddard Space Flight Center, Greenbelt, MD. The first author gratefully acknowledges assistance from the Australian-American Fulbright Commission and the NASA Earth and Space Science Fellowship Program. This work was also supported by NSF Grants OCE-0725476 (JS) and OCE-0850350 (SG). Finally, we wish to thank three anonymous reviewers, whose suggestions improved the quality of this manuscript.

## APPENDIX

### Data Validation and Compositing Procedure

#### *a. Comparison between Argo and mooring data*

Figure A1a shows temperature observations over our study period (2004–10) at a RAMA mooring in the Indian Ocean at 0°N, 90°E (McPhaden et al. 2009). For comparison, Fig. A1b shows temperatures from nearby Argo profiles. It is evident that the distribution of Argo data is much more sparse in time; however, by comparing time periods with overlapping data, it can be seen that Argo observations capture the same variability as do the RAMA temperatures (e.g., cooling below 30 m in 2007 and a transition to warm conditions throughout the top 80 m in 2010). Figures A1c,d illustrate that densities, and thus estimates of MLD, from Argo are also comparable to those from the RAMA mooring. Moreover, Argo profiles typically have higher vertical resolution in the upper ocean than do mooring data, particularly around the level of the mixed layer base, which means that individual MLD estimates from Argo are more accurate than those from moorings.

#### *b. Methodology for compositing Argo profile data*

To estimate the composite MJO signal from Argo measurements, we extracted all profiles within a grid box defined by  $(x_g \pm \Delta x, y_g \pm \Delta y)$  and made within  $\pm \Delta t = 12$  days of the significant MJO events during a given phase, and fit a model to the data from those profiles. Although not a true oscillation, the MJO signal is roughly sinusoidal in shape over one cycle (e.g., Waliser et al. 2003; Schiller and Godfrey 2003; Sato et al. 2011). Locally, this can be approximated as quadratic in time, so we modeled each phase of the MJO signal at each grid point  $(x_g, y_g)$  using

$$A = A_o + \alpha_1 t' + \alpha_2 t'^2 + \beta x' + \gamma y' + \eta(\text{soi}). \quad (\text{A1})$$

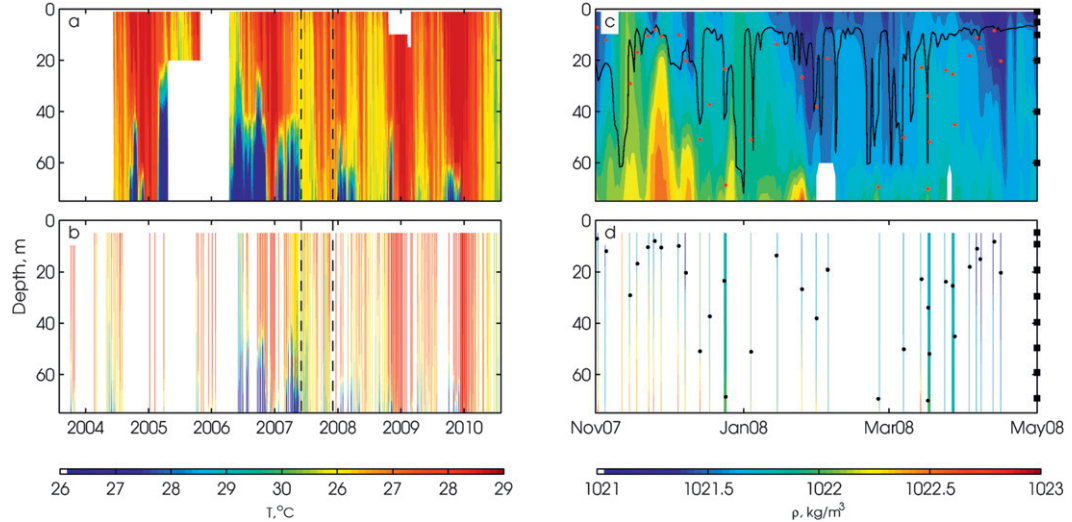


FIG. A1. Comparison of (top) upper-ocean data from a RAMA mooring at  $(0^\circ, 90^\circ\text{E})$  and (bottom) data from all Argo profiles made in a  $8^\circ$  (longitude)  $\times 4^\circ$  (latitude) box surrounding the mooring site. (a),(b) Temperature from 2004–10. Density for one winter season [November 2007–April 2008; indicated with dashed lines in (a),(b)] shows the density for the (c) same RAMA data and (d) Argo profiles. In (c), the depths of the salinity sensors at this mooring are shown with black squares, and in (d) the vertical sampling of a typical Argo profile is shown with squares. The MLD, calculated using a density threshold criterion, is superimposed on the densities: the TAO data-derived MLDs are plotted as a black line in (c), and the Argo-derived MLDs are plotted as black dots in (d). For comparison, the Argo MLDs are also plotted as red dots in (c).

A robust linear least squares fitting technique was used to evaluate this expression for each of the quantities  $A$  that were derived from the Argo profile data (i.e.,  $T$ ,  $h$ ,  $\partial T/\partial z$ ,  $\Delta T$ ). In Eq. (A1),  $t'$  represents the time difference between each Argo profile and the nearest significant MJO event, and  $x'$  and  $y'$  give the distance from the profile to the center of the grid box. The fit yielded the following quantities:  $A_o$ , the composite variation of  $A$  associated with the MJO;  $\alpha_1$  and  $\alpha_2$ , the MJO temporal tendency;  $\beta$  and  $\gamma$ , the MJO-related spatial variation of  $A$  over the grid box; and  $\eta$ , which accounted for the interannual variations in  $A$  resulting from ENSO. This last term was multiplied by the Southern Oscillation index (SOI; Trenberth 1984), to which a 120-day low-pass filter had been applied to exclude high-frequency variations.

The regression procedure is illustrated in Fig. A2, which shows the Argo mixed layer temperature data in the grid box centered at  $(x_g, y_g) = (0^\circ\text{N}, 90^\circ\text{E})$ , that is, the same location shown in Fig. A1. The top panels illustrate the typical scatter of profile locations for each phase of the MJO. The second row of panels (Fig. A2b) shows the deseasonalized temperature ( $\hat{T}$ ) of each profile in the grid box (i.e., surface-level data in Fig. A1b), plotted against the time from the profile to the nearest large MJO event ( $t'$ ). The change in temperature through the progression of the MJO cycle is clear: in phase 1, the temperature anomaly is near its maximum (as indicated by the square markers at  $t' = 0$ );

accordingly, the fit [solid line; Eq. (A1)] yields a positive inflection point (Fig. A2b). Phases 2–3 show decreasing temperatures; consistent with this, the fits to these data have negative slopes ( $\partial T/\partial t < 0$ ). The minimum MJO temperature anomaly occurs in phases 4–5, consistent with negative inflection points in the fits. The temperature increases in phases 6–8, and the fits give positive slopes. For comparison, Fig. A2c shows the satellite-derived SST from TMI (Table 1) in the same grid box. Although there are many more satellite SST observations than Argo profiles, the fits to both sets of data are similar, illustrating that the Argo dataset does a good job of capturing the MJO temperature signal. A comparison of the fits to the gridded SST with the fits to the Argo mixed layer temperature, at all grid points for which the magnitude of the OLR anomaly exceeds  $10 \text{ W m}^{-2}$  and for all MJO phases, gives a significant correlation ( $R^2 = 0.3$  for the mean and  $R^2 = 0.5$  for the  $\alpha_1$  term, cf. a 95% significance level of  $R^2 = 0.01$ ). This shows that Argo data, though sparse, can effectively capture the variability associated with the canonical MJO.

Finally, Fig. A2d shows the deseasonalized MLD estimates from Argo (i.e., black dots in Fig. A1d) and the regressions to these data. Though the scatter for the MLD is greater than that for the mixed layer temperature data shown in Fig. A2b, there is still a clear MLD signal throughout the life cycle of the MJO, with negative anomalies (shallow mixed layers) in phases 8 and 1

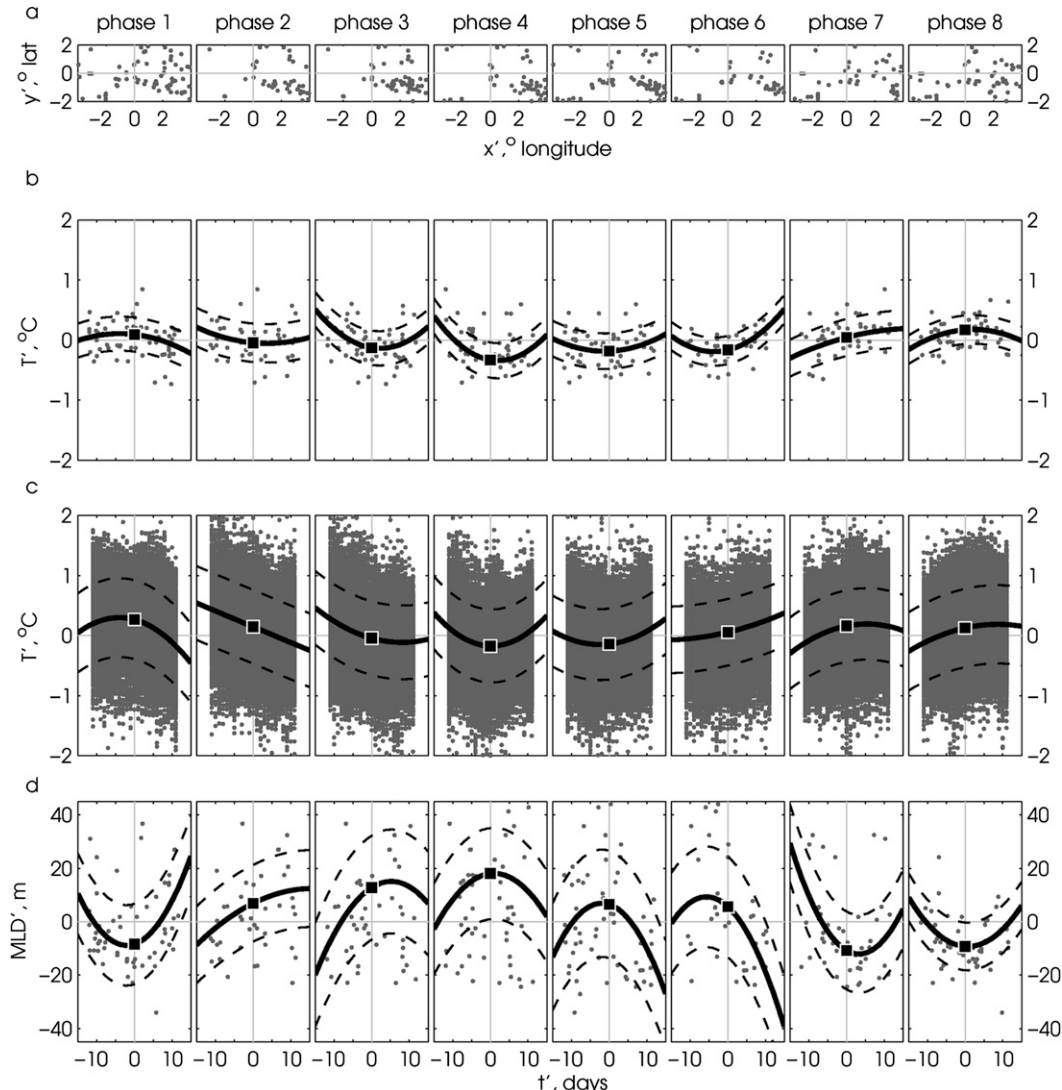


FIG. A2. Example of regressions to Argo data in one grid box ( $0^\circ \pm 2^\circ\text{N}$ ,  $90^\circ \pm 4^\circ\text{E}$ ). (a) For each phase, the geographical scatter of the Argo profiles in the grid box are shown. (b) The deseasonalized mixed layer temperature anomaly for each profile in the grid box, plotted against the time difference between the profile measurement and the nearest significant MJO event in that phase ( $t'$ ). The black squares and lines result from the robust fit to the data [Eq. (A1)], with the squares indicating the mean temperature anomaly ( $T_o$ ) and the solid (dashed) lines showing the fit to the data ( $\pm$  the standard deviation). (c) SST measurements derived from the TMI satellite product in the same grid box, with the fit and standard deviation of the data. (d) As in (b), but show regressions to MLD anomalies.

consistent with suppressed conditions (warm surface temperatures), and the peak positive MLD anomaly in phase 4 consistent with active conditions (surface cooling). These panels illustrate that although the MLD observations from Argo at a given location are temporally sparse (Fig. A1d), a significant and consistent signal emerges when the data from many events are combined and fit to Eq. (A1).

The spatial and temporal derivatives of  $T$  and  $h$  that emerge from the fit in Eq. (A1) provide the gradient terms used in the heat budget [Eq. (2)]. From the fits

to mixed layer temperature,  $\alpha_1$ ,  $\beta$ , and  $\gamma$  give the terms  $\partial T/\partial t$ ,  $\partial T/\partial x$ , and  $\partial T/\partial y$ , respectively. Similarly,  $\partial h/\partial t$  was extracted from the fit to MLD.

We found that a value of  $\Delta t = 12$  days, corresponding to around one quarter of the MJO cycle, yielded the best fits to the Argo data. For  $\Delta t < 12$  days, the fit was poor and the temporal evolution of the MJO signal was not well captured, and conversely for  $\Delta t$  much larger than 12 days, a quadratic fit was not able to adequately capture the variance. We used grid boxes defined by  $\Delta x = 4^\circ$  and  $\Delta y = 2^\circ$ , which maximizes the number of profile data

that go into the regressions while capturing the spatial variation of the MJO. In most regions, the results of the analysis were not sensitive to the size of the grid box: generally, larger grid boxes resulted in smoother spatial patterns and composite signals with slightly smaller amplitudes. The exception was the far western Pacific Ocean, where the spatial scale of MJO variations is small, so using larger grid boxes resulted in a large noise-to-signal ratio, but smaller boxes contained few profiles and robust composites could not be estimated.

## REFERENCES

- Anderson, S., R. Weller, and R. Lukas, 1996: Surface buoyancy forcing and the mixed layer of the western Pacific warm pool: Observations and 1D model results. *J. Climate*, **9**, 3056–3085.
- Ardizzone, J., R. Atlas, R. Hoffman, J. Jusem, S. Leidner, and D. Moroni, 2009: New multiplatform ocean surface wind product available. *Eos, Trans. Amer. Geophys. Union*, **90**, 231.
- Bellenger, H., and J. Duvel, 2009: An analysis of tropical ocean diurnal warm layers. *J. Climate*, **22**, 3629–3646.
- Bernie, D., S. Woolnough, J. Slingo, and E. Guilyardi, 2005: Modeling diurnal and intraseasonal variability of the ocean mixed layer. *J. Climate*, **18**, 1190–1202.
- , E. Guilyardi, G. Madec, J. Slingo, S. Woolnough, and J. Cole, 2008: Impact of resolving the diurnal cycle in an ocean-atmosphere GCM. Part 2: A diurnally coupled CGCM. *Climate Dyn.*, **31**, 909–925, doi:10.1007/s00382-008-0429-z.
- Bonjean, F., and G. S. E. Lagerloef, 2002: Diagnostic model and analysis of the surface currents in the tropical Pacific Ocean. *J. Phys. Oceanogr.*, **32**, 2938–2954.
- Cronin, M., and M. McPhaden, 1997: The upper ocean heat balance in the western equatorial Pacific warm pool during September–December 1992. *J. Geophys. Res.*, **102** (C4), 8533–8553.
- , and —, 2002: Barrier layer formation during westerly wind bursts. *J. Geophys. Res.*, **107** (C12), 2101–2112.
- de Boyer Montégut, C., G. Madec, A. Fischer, A. Lazar, and D. Iudicone, 2004: Mixed layer depth over the global ocean: An examination of profile data and a profile-based climatology. *J. Geophys. Res.*, **109**, C12003, doi:10.1029/2004JC002378.
- , J. Mignot, A. Lazar, and S. Cravatte, 2007: Control of salinity on the mixed layer depth in the world ocean: 1. General description. *J. Geophys. Res.*, **112**, C06011, doi:10.1029/2006JC003953.
- Duncan, B., and W. Han, 2009: Indian Ocean intraseasonal sea surface temperature variability during boreal summer: Madden-Julian Oscillation versus submonthly forcing and processes. *J. Geophys. Res.*, **114**, C05002, doi:10.1029/2008JC004958.
- Duvel, J., and J. Vialard, 2007: Indo-Pacific sea surface temperature perturbations associated with intraseasonal oscillations of tropical convection. *J. Climate*, **20**, 3056–3082.
- , R. Roca, and J. Vialard, 2004: Ocean mixed layer temperature variations induced by intraseasonal convective perturbations over the Indian Ocean. *J. Atmos. Sci.*, **61**, 1004–1023.
- Flatau, M., P. Flatau, P. Phoebus, and P. Niiler, 1997: The feedback between equatorial convection and local radiative and evaporative processes: The implications for intraseasonal oscillations. *J. Atmos. Sci.*, **54**, 2373–2386.
- Gregg, W., 2008: Assimilation of SeaWiFS ocean chlorophyll data into a three-dimensional global ocean model. *J. Mar. Syst.*, **69** (3–4), 205–225.
- Han, W., D. Yuan, W. Liu, and D. Halkides, 2007: Intraseasonal variability of Indian Ocean sea surface temperature during boreal winter: Madden-Julian Oscillation versus submonthly forcing and processes. *J. Geophys. Res.*, **112**, C04001, doi:10.1029/2006JC003791.
- Hendon, H., and M. Salby, 1994: The life cycle of the Madden-Julian Oscillation. *J. Atmos. Sci.*, **51**, 2225–2237.
- , and J. Glick, 1997: Intraseasonal air-sea interaction in the tropical Indian and Pacific Oceans. *J. Climate*, **10**, 647–661.
- Inness, P., and J. Slingo, 2003: Simulation of the Madden-Julian oscillation in a coupled general circulation model. Part I: Comparison with observations and an atmosphere-only GCM. *J. Climate*, **16**, 345–364.
- Jayakumar, A., J. Vialard, M. Lengaigne, C. Gnanaseelan, J. P. McCreary, and P. Kumar, 2011: Processes controlling the surface temperature signature of the Madden-Julian Oscillation in the thermocline ridge of the Indian Ocean. *Climate Dyn.*, **37** (11–12), 2217–2234, doi:10.1007/s00382-010-0953-5.
- Johnson, E., F. Bonjean, G. Lagerloef, J. Gunn, and G. Mitchum, 2007: Validation and error analysis of OSCAR sea surface currents. *J. Atmos. Oceanic Technol.*, **24**, 688–701.
- Kanamitsu, M., W. Ebisuzaki, J. Woollen, S. Yang, J. Hnilo, M. Fiorino, and G. Potter, 2002: NCEP-DOE AMIP-II Reanalysis (R-2). *Bull. Amer. Meteor. Soc.*, **83**, 1631–1643.
- Kessler, W., M. McPhaden, and K. Weickmann, 1995: Forcing of intraseasonal Kelvin waves in the equatorial Pacific. *J. Geophys. Res.*, **100** (C6), 10 613–10 631.
- Kubota, M., N. Iwasaka, S. Kizu, M. Konda, and K. Kutsuwada, 2002: Japanese ocean flux data sets with use of remote sensing observations (J-OFURO). *J. Oceanogr.*, **58**, 213–225.
- Kumar, B. P., J. Vialard, M. Lengaigne, V. Murty, and M. McPhaden, 2011: TropFlux: Air-sea fluxes for the global tropical oceans—Description and evaluation against observations. *Climate Dyn.*, doi:10.1007/s00382-011-1115-0, in press.
- Lau, W., and D. Waliser, 2005: *Intraseasonal Variability in the Atmosphere–Ocean Climate System*. Springer, 474 pp.
- Liebmann, B., and C. A. Smith, 1996: Description of a complete (interpolated) outgoing longwave radiation dataset. *Bull. Amer. Meteor. Soc.*, **77**, 1275–1277.
- Lucas, L., D. Waliser, and R. Murtugudde, 2010: Mechanisms governing sea surface temperature anomalies in the eastern tropical Pacific Ocean associated with the boreal winter Madden-Julian Oscillation. *J. Geophys. Res.*, **115**, C05012, doi:10.1029/2009JC005450.
- Lukas, R., and E. Lindstrom, 1991: The mixed layer of the western equatorial Pacific Ocean. *J. Geophys. Res.*, **96**, 3343–3357.
- Madden, R., and P. Julian, 1972: Description of global-scale circulation cells in the tropics with a 40–50 day period. *J. Atmos. Sci.*, **29**, 1109–1123.
- Maloney, E., and J. Kiehl, 2002: MJO-related SST variations over the tropical eastern Pacific during Northern Hemisphere summer. *J. Climate*, **15**, 675–689.
- , and A. Sobel, 2004: Surface fluxes and ocean coupling in the tropical intraseasonal oscillation. *J. Climate*, **17**, 3717–3720.
- Matthews, A. J., P. Singhru, and K. J. Heywood, 2010: Ocean temperature and salinity components of the Madden-Julian oscillation observed by Argo floats. *Climate Dyn.*, **35** (7), 1149–1168, doi:10.1007/s00382-009-0631-7.
- McPhaden, M. J., 2002: Mixed layer temperature balance on intraseasonal timescales in the equatorial Pacific Ocean. *J. Climate*, **15**, 2632–2647.

- , and Coauthors, 2009: RAMA: The Research Moored Array for African–Asian–Australian Monsoon Analysis and Prediction. *Bull. Amer. Meteor. Soc.*, **90**, 459–480.
- Morel, A., and D. Antoine, 1994: Heating rate within the upper ocean in relation to its biooptical state. *J. Phys. Oceanogr.*, **24**, 1652–1665.
- Resplandy, L., J. Vialard, M. Lévy, O. Aumont, and Y. Dandonneau, 2009: Seasonal and intraseasonal biogeochemical variability in the thermocline ridge of the southern tropical Indian Ocean. *J. Geophys. Res.*, **114**, C07024, doi:10.1029/2008JC005246.
- Roemmich, D., and J. Gilson, 2009: The 2004–2008 mean and annual cycle of temperature, salinity, and steric height in the global ocean from the Argo program. *Prog. Oceanogr.*, **82** (2), 81–100.
- Saji, N., S. Xie, and C. Tam, 2006: Satellite observations of intense intraseasonal cooling events in the tropical south Indian Ocean. *Geophys. Res. Lett.*, **33**, L14704, doi:10.1029/2006GL026525.
- Sato, N., K. Yoneyama, Y. Takayabu, R. Shirooka, and M. Yoshizaki, 2011: Variability of the oceanic surface and subsurface layers in the warm pool associated with the atmospheric northward-propagating intraseasonal variability. *Deep-Sea Res. II*, **57** (13–14), 1201–1211, doi:10.1016/j.dsr2.2009.12.009.
- Schiller, A., and J. Godfrey, 2003: Indian Ocean intraseasonal variability in an ocean general circulation model. *J. Climate*, **16**, 21–39.
- Seo, K.-H., W. Wang, J. Gottschalck, Q. Zhang, J.-K. E. Schemm, W. R. Higgins, and A. Kumar, 2009: Evaluation of MJO forecast skill from several statistical and dynamical forecast models. *J. Climate*, **22**, 2372–2388.
- Shinoda, T., 2005: Impact of the diurnal cycle of solar radiation on intraseasonal SST variability in the western equatorial Pacific. *J. Climate*, **18**, 2628–2636.
- , and H. Hendon, 1998: Mixed layer modeling of intraseasonal variability in the tropical western Pacific and Indian Oceans. *J. Climate*, **11**, 2668–2685.
- , and —, 2001: Upper-ocean heat budget in response to the Madden–Julian Oscillation in the western equatorial Pacific. *J. Climate*, **14**, 4147–4165.
- , —, and J. Glick, 1998: Intraseasonal variability of surface fluxes and sea surface temperature in the tropical western Pacific and Indian Oceans. *J. Climate*, **11**, 1685–1702.
- Simmons, A., S. Uppala, D. Dee, and S. Kobayashi, 2007: ERA-Interim: New ECMWF reanalysis products from 1989 onwards. *ECMWF Newsletter*, No. 110, ECMWF, Reading, United Kingdom, 25–35.
- Sprintall, J., and M. McPhaden, 1994: Surface layer variations observed in multiyear time series measurements from the western equatorial Pacific. *J. Geophys. Res.*, **99**, 963–979.
- Sweeney, C., A. Gnanadesikan, S. Griffies, M. Harrison, A. Rosati, and B. Samuels, 2005: Impacts of shortwave penetration depth on large-scale ocean circulation and heat transport. *J. Phys. Oceanogr.*, **35**, 1103–1119.
- Trenberth, K. E., 1984: Signal versus noise in the Southern Oscillation. *Mon. Wea. Rev.*, **112**, 326–332.
- Vialard, J., and P. Delecluse, 1998: An OGCM study for the TOGA decade. Part II: Barrier-layer formation and variability. *J. Phys. Oceanogr.*, **28**, 1089–1106.
- , G. Foltz, M. McPhaden, J. Duvel, and C. de Boyer Montégut, 2008: Strong Indian Ocean sea surface temperature signals associated with the Madden–Julian Oscillation in late 2007 and early 2008. *Geophys. Res. Lett.*, **35**, L19608, doi:10.1029/2008GL035238.
- Vinayachandran, P., and N. Saji, 2008: Mechanisms of south Indian Ocean intraseasonal cooling. *Geophys. Res. Lett.*, **35**, L23607, doi:10.1029/2008GL035733.
- Waliser, D. E., K. Lau, and J. Kim, 1999: The influence of coupled sea surface temperatures on the Madden–Julian oscillation: A model perturbation experiment. *J. Atmos. Sci.*, **56**, 333–358.
- , R. Murtugudde, and L. Lucas, 2003: Indo-Pacific Ocean response to atmospheric intraseasonal variability: 1. Austral summer and the Madden–Julian Oscillation. *J. Geophys. Res.*, **108**, 3160, doi:10.1029/2002JC001620.
- , —, P. Strutton, and J.-L. Li, 2005: Subseasonal organization of ocean chlorophyll: Prospects for prediction based on the Madden–Julian Oscillation. *Geophys. Res. Lett.*, **32**, L23602, doi:10.1029/2005GL024300.
- Wheeler, M., and H. Hendon, 2004: An all-season real-time multivariate MJO index: Development of an index for monitoring and prediction. *Mon. Wea. Rev.*, **132**, 1917–1932.
- Woolnough, S. J., J. M. Slingo, and B. J. Hoskins, 2000: The relationship between convection and sea surface temperature on intraseasonal timescales. *J. Climate*, **13**, 2086–2104.
- , F. Vitart, and M. Balmaseda, 2007: The role of the ocean in the Madden–Julian Oscillation: Implications for MJO prediction. *Quart. J. Roy. Meteor. Soc.*, **133**, 117–128.
- Yu, L., and R. Weller, 2007: Objectively analyzed air–sea heat fluxes for the global ice-free oceans (1981–2005). *Bull. Amer. Meteor. Soc.*, **88**, 527–539.
- Zhang, C., 2005: Madden–Julian Oscillation. *Rev. Geophys.*, **43**, RG2003, doi:10.1029/2004RG000158.
- , and M. J. McPhaden, 2000: Intraseasonal surface cooling in the equatorial western Pacific. *J. Climate*, **13**, 2261–2276.
- Zhang, G. J., and M. J. McPhaden, 1995: The relationship between sea surface temperature and latent heat flux in the equatorial Pacific. *J. Climate*, **8**, 589–605.
- Zhang, Y., W. Rossow, A. Lacis, V. Oinas, and M. Mishchenko, 2004: Calculation of radiative fluxes from the surface to top of atmosphere based on ISCCP and other global data sets: Refinements of the radiative transfer model and the input data. *J. Geophys. Res.*, **109**, D19105, doi:10.1029/2003JD004457.